High-Resolution structures of microtubule-bound KIF1A and its pathogenic variant P305L

Matthieu P.M.H. Benoit[1,*], Lu Rao[1,*], Ana B. Asenjo[1], Arne Gennerich[1,#], and Hernando Sosa[1,#]

[1] Department of Biochemistry and Gruss-Lipper Biophotonics Center, Albert Einstein College of Medicine, Bronx, NY 10461

[*] M.P.M.H. Benoit and L. Rao contributed equally to the paper.

[#] Correspondence: arne.gennerich@einsteinmed.edu and hernando.sosa@einsteinmed.edu

Running head: High-resolution structures of KIF1A

Abstract

Mutations in the Kinesin-3 motor KIF1A, a microtubule (MT)-associated motor protein, cause devastating neurodevelopmental and neurodegenerative diseases termed KIF1A-associated neurological disorders (KAND). While the mechanism of KIF1A is increasingly understood, high resolution (<4 Å) structural information of KIF1A-MT complexes is lacking. Here, we present 2.7-3.4 Å resolution structures of dimeric MT-bound wild-type (WT) KIF1A and the pathogenic P305L mutant as a function of the nucleotide state. Our structures reveal that 1) the KIF1A dimer binds MTs in one- and two-heads-bound states, 2) that both MT-bound heads assume distinct conformations with tight inter-head connection, 3) the position and conformation of the class-specific loop 12 (the K-loop), and 4) that the P305L mutation causes structural changes in the K-loop that result in a weakly MT-bound state. Motivated by our structural insights, we performed structure-function studies that reveal that both the K-loop and head-head coordination are major determinants of KIF1A's superprocessive motility. Our work provides key insights into the mechanism of KIF1A and provides near-atomic structures of WT and mutant KIF1A for future structure-guided drug-design approaches to treat KAND.

Introduction

KIF1A is a neuron-specific member of the kinesin-3 family of microtubule (MT) plus-end-directed motor proteins that powers the migration of nuclei in differentiating brain stem cells[1,2] and the transport of synaptic precursors and dense core vesicles to axon terminals[3-8]. Its dysfunction contributes to severe neurodevelopmental and neurodegenerative diseases termed KIF1A-associated neurological disorders (KAND), including progressive spastic paraplegias, microcephaly, encephalopathies, intellectual disability, autism, autonomic and peripheral neuropathy, optic nerve atrophy, cerebral and cerebellar atrophy, and others[9-51]. To date, more than 145 inherited and *de novo* KAND mutations have been identified, and these mutations span the entirety of the KIF1A protein sequence[9]. The majority are located within the motor domain (MD or 'head')[9] and are thus predicted to affect the motor's motility properties whereas mutations located outside the MD are likely involved in mediating dimerization, autoinhibition, and/or cargo binding[10]. Our own work[9,52] and the work of others[53,54] has indeed shown that KAND MD mutations affect the motor's ability to generate force and movement.

Through the patient advocacy group *KIF1A.org*, more than 500 families with children and adults with KIF1A mutations have come together to improve the lives of those affected by KAND and to accelerate drug discovery. Unfortunately, the molecular etiologies of KAND remain poorly understood, in part because KIF1A's molecular mechanism remains unclear. For example, KIF1A is extremely fast and super-processive (the motor can take more than a thousand steps before dissociating), and at the same time, gives up easily under load. These behaviors distinguish KIF1A from the founding member of the kinesin family, kinesin 1, and it remains unknown how KIF1A achieves this unique set of properties. In addition, while most mutations occur in KIF1A's MD[9], high-resolution (< 4 Å) structures of the KIF1A-MT complex do not exist. Targeted therapies

require knowledge of the nucleotide state-dependent structures of KIF1A and how disease mutations affect KIF1A's conformational states. This knowledge will aid the design of drugs with increased specificity for the mutant proteins.

While the MD of KIF1A is highly conserved among the members of the kinesin superfamily[55,56], it contains distinct structural elements that may explain KIF1A's unique set of properties. KIF1A's positively charged loop 12 (called the "K-loop" due to the presence of the sequence KNKKKKK) facilitates KIF1A's initial binding to the MT[57] and is responsible for the motor's ability to rapidly reattach to the MT following detachment under load, a property that results in a unique sawtooth-like clustering of force generation events[52]. However, our understanding of the unique motile properties of KIF1A is still limited due the lack of high-resolution structural information of the KIF1A-MT complex. The KIF1A motor domain has been visualized in a variety of experimental conditions by X-ray crystallography[58-61] and in complex with MTs at medium resolution (6-15 Å) using cryoEM[58,62-64]. However, structures of KIF1A-MT complexes at higher resolution are needed to detect small but functionally important conformational changes that occur with the formation of the KIF1A-MT complex. High resolution is essential to unambiguously trace the polypeptide chains and to determine the position of side chains for structure-guided drug discovery efforts[65,66]. Furthermore, in previous structural work, the functionally important K-loop remained mostly unresolved and there is no structural information on MT-bound KIF1A dimers, the functional oligomeric form required for unidirectional processive motility[67,68].

To address these issues, we present here the high resolution (2.7-3.4 Å overall resolution) cryo-EM structures of dimeric KIF1A bound to MTs in the presence of the non-hydrolysable ATP analogue, AMP-PNP (adenylyl-imidodiphosphate), in the presence of ADP and in the absence of

nucleotides (Apo-state) to mimic distinct steps of the KIF1A-MT ATPase cycle. The structures show the entire K-loop and we provide functional evidence for its critical role in KIF1A's superprocessivity. We also provide structural and functional evidence that the two motor domains of KIF1A are coordinated and that coordination between both motor domains contributes to the motor's processive motion. Finally, to aid drug development, we solved the near-atomic resolution structure of the P305L KAND mutant bound to MTs and provide structural insights into the deleterious effects that this mutation has on KIF1A function.

In summary, our work provides key insights into the mechanism of KIF1A and demonstrates the possibility to solve high-resolution structures of MT-bound KAND mutants, which opens-up the development of therapeutics based mutant structures.

Results

High-resolution structures of the KIF1A microtubule complexes

To understand the structural basis of the unique motile properties of KIF1A and determine the structural effects of KIF1A missense mutations associated with neurological diseases (KANDs), we determined the high resolution cryo-EM structures (2.7-3.4 Å overall resolution) of dimeric KIF1A (Supplementary Fig. 5) bound to microtubules (MTs) in different nucleotide states to mimic different points of its ATPase cycle. Classification and refinement procedure were applied to the cryo-EM data to separate distinct conformations of the two motor domains of KIF1A in the MT-bound complexes (Supplementary Fig 2-3, Fig.1).

In the presence of AMP-PNP (ANP used here as abbreviation for AMP-PNP in the map and model names), the dominant classes display two motor domains joined by KIF1A's coiled-coil dimerization domain and bound to two contiguous tubulin heterodimers along an MT protofilament (Fig. 1a). The motor domain closer to the MT plus-end and in the direction of movement (the leading head) has a backward oriented neck-linker and an open nucleotide binding pocket while the trailing head has a docked forward oriented neck-linker and a closed nucleotide binding pocket (Figs. 1a and 2a). Both the leading and trailing heads have AMP-PNP bound in the nucleotide-binding pocket. Other classes include single MT bound heads with a trailing-like head and a missing leading head or with the trailing head of another dimer occupying the leading position (Supplementary Figs. 2 and 3). The classification also revealed that the trailing head assumed three different conformations (Supplementary. Fig. 3). Two of the classes were very similar to each other (MT-KIF1A-ANP-T_2L_1 and MT-KIF1A-ANP-T_3L_1) and were averaged to produce the map shown in Fig. 1a (MT-KIF1A-ANP-$T_{23}L_1$). This map was used to build the atomic model of the KIF1A-ANP average two-heads-bound state (Fig. 2a). The most distinct of

these conformations appeared only in single-head-bound classes and showed a conformation with the nucleotide-binding pocket not fully closed (Supplementary Fig. 3). This not fully closed conformation suggests that the binding of the partner motor domain in the leading position helps stabilizing the closed conformation in the trailing head . This is evidence for enhanced coordination between the motor domains as the closed catalytic-competent conformation is stabilized after the partner motor domain is bound to the MT in the leading position and in the open conformation.

In the presence of ADP or the absence of nucleotides (Apo state) only classes with single MT-bound heads were observed with no visible connection to the partner motor domains (Fig. 1b,c). This indicates a configuration where one head is MT-bound and the partner head is MT-unbound and mobile. The structure of the MT-bound motor domain was similar in both conditions except for the presence or absence of ADP in the nucleotide-binding pocket (Figs. 1b-c and 2b-c).

The open and closed conformations refer to distinct conformations of the nucleotide-binding pocket observed in MT-bound kinesins[69,70]. These conformations are characterized by the distance between key residues involved in nucleotide binding with the largest and shortest distances defining respectively the open and closed conformations (Fig. 3). Semi-closed (or semi-open) conformations displays intermediate distance values between the open are closed conformations and are observed in the crystal structures of MT-unbound free kinesins with ADP in the nucleotide-binding pocket. The open conformation observed in the high-resolution MT-KIF1A complexes in the ADP and Apo states as well as in the leading head with AMP-PNP in the active site, represents a novel KIF1A motor domain conformation that to our knowledge has not been shown previously either in X-ray crystallography-based models or in models of KIF1A-MT complexes derived from lower resolution (>6 Å) cryo-EM data. All the previous KIF1A motor domain structures can be classified as either closed or semi-closed conformations (Fig. 3d). The

difference between our observations and previous cryo-EM results likely arises from the resolution differences of the cryo-EM data on which the models are based. The open and semi-closed conformations at lower resolution would appear very similar and hard to differentiate. The comparison between the crystal structures and the high-resolution KIF1A-MT complexes suggests that the opening of the KIF1A nucleotide-binding pocket is a direct consequence of MT binding. This conformational change from a semi-closed to an open conformation provides a structural basis for the acceleration of ADP release typically associated with kinesin MT binding[71].

Structure and role of the KIF1A-sepcific K-loop

KIF1A, like other kinesin-3 family members, has an elongated Lys-rich loop-12 referred to as the K-loop. While it has been shown that the K-loop is important for KIF1A-MT binding[72-75], how it interacts with MTs has not been clear as most of this loop is either disordered or not resolved in X-ray crystal structures of KIF1A and in lower resolution cryo-EM structures of KIF1A-MT complexes. Our high-resolution structures of KIF1A-MT complexes show the complete polypeptide path of the K-loop (Fig. 3a). Near the tip of the loop, the maps are noisier and at a lower resolution than in other areas of the complex, indicating higher mobility in this area. The lower resolution hindered a clear identification of the side-chain positions in these areas, but it still enabled us to determine of the overall path of the polypeptide chain. In all maps, the K-loop projects outwards from the side of the motor domain opposite to the nucleotide-binding site between KIF1A's helix-4 and the β-tubulin C-terminal helix (helix-12). The most N-terminal lysines in the K-loop (K299 and K300) are positioned close to the end of the β-tubulin terminal helix (Helix-12) so that they could potentially form electrostatic interactions with β-tubulin Asp-427. Interestingly, other kinesin-3s such as KIF14 (Fig. 3b,c), have also conserved positively-

charged residues in this area despite having a shorter loop-12 with less overall positively-charged residues. This raises the possibility that electrostatic interactions between this area of loop-12 and the MT surface are highly critical for KIF1A motility.

To explore this possibility, we made a chimeric construct (Fig. 3c) where KIF1A's K-loop was swapped for the loop-12 of *Hs*KIF14 (K-swap). In near-physiological ionic strength buffer (BRB80, see methods), while the K-swap construct moves on average at a slightly higher velocity than WT KIF1A (Fig. 3d,e), its run-length it greatly reduced (2.7 µm instead of 14.6 µm; median values) to a value comparable to the run length of kinesin-1 KIF5B, which does not have a K-loop (Fig. 3d,f). These results show that the KIF1A K-loop and the less positively charged loop-12 of KIF14 are not functionally equivalent and that an intact K-loop is necessary for the characteristic long run length of KIF1A. This is consistent with a recent study showing that the KIF1A run length scales with the number of positively charged residues in the K-loop[75]. These results appear difficult to reconcile with the fact that most of the K-loop lysines in the structures of the KIF1A-MT complexes appear far from the MT surface or the rest of the kinesin motor domain (Fig. 3). However, the results can be reconciled if one considers that the KIF1A motor domain can bind to the MT in two distinct modalities, one represented by the structures of the cryo-EM complex shown in Figures 1 and 2 where the motor domain is bound to the MT in a relatively rigid and stereospecific manner and another more mobile and flexible binding mode mediated by electrostatic interactions between the K-loop and the polyglutamated tubulin C-terminal tails[73]. Removing all or part of the charged residues of the K-loop would impair this binding mode and consequently any motility parameter that reports on the ability of the KIF1A motor to maintain its grip on the MT track, such as run length. The flexibility and transient nature of this binding mode would make it difficult to resolve in the cryo-EM maps but we find evidence for it in the structures

of the KIF1A P305L mutant in complex with MTs (see below).

Conformation of the KIF1A Neck-linker

The conformation and position of the neck-linker is another notable difference between the high-resolution structures of the KIF1A-MT complex and other kinesin-MT complexes. In the MT two-heads-bound state (MT-KIF1A-ANP-$T_{23}L_1$), the path of the neck-linkers of the leading and trailing heads is different from the one observed in the structures of the KIF14-MT complex[70] (the only other available high-resolution structures of a kinesin in the two-heads-bound state). In the KIF1A two-heads-bound state, the neck-linkers are more separated from the motor domain and adopt a more direct and straighter path between the two motor domains. This difference arises from sequence variations between the neck-linkers of the different kinesins. KIF1A and other kinesin-3s, but not KIF14, have a family-conserved proline residue that is the first residue of the α-helix that forms the coiled-coil dimerization domain in KIF1A (Fig. 4). This makes the KIF1A neck-linker shorter by two to four residues than the neck-linkers of KIF5B or KIF14 (Fig. 4d). As the length of the neck-linker has been shown to affect kinesin processivity[76], we surmise that the tighter KIF1A neck-linkers in the two-heads-bound state also results in tighter coordination between their catalytic cycles and therefore in an increased processivity of the motor. To test this hypothesis, we measured the velocity and run-length of a KIF1A construct where the conserved proline residue, which marks the start of the coiled coil-helix, is replaced by a leucine (P364L), a residue found at the same position in human KIF5B (L335) and other kinesins (Fig. 4d). We found that while the P364L mutation did not affect the velocity of the motor (Fig. 3d,e), it resulted in a small but significant reduction in run length (10.2 µm instead of 14.6 µm median length, Fig. 3d,f), implying that the likely more strained neck-linkers of KIF1A also contribute to the motor's high

processivity. Our results therefore suggests that KIF1A's K-loop and its neck-linkers are both evolutionary adopted for an increased MT affinity and an improved coordination between the motor domains, resulting in a high MT on-rate and the exceptionally high processivity of the motor.

High-resolution structures of KIF1A with KAND-associated missense mutation P305L

To aid future structure-based drug developments, we also determined high-resolution structures of KIF1A bearing the KAND-associated mutation P305L in complex with MTs in the same nucleotide conditions as for MT-bound WT KIF1A described in the previous sections (Fig. 1). To obtain enough MT decoration with the P305L mutant protein for cryo-EM imaging, a higher ratio of kinesin to MTs and a lower ionic strength buffer were required compared to the conditions used for the WT protein (Supplementary Table 1). Even under these conditions, the level of decoration was lower than obtained for WT KIF1A. This observation is consistent with our previous study that demonstrated impaired MT-binding of the P305L mutant[77].

As WT KIF1A, the KIF1A-P305L mutant produced classes that display a two-heads-bound conformation with a leading head in the open conformation and a trailing head in the closed conformation in the presence of AMP-PNP (MT-KIF1A^{P305L}-ANP-TL$_1$, Fig 5a, Supplementary Fig. 4) and single MT-bound head in the open conformation in the ADP and Apo states (Fig. 5b,c). The P305L mutant in the ADP state produces a distinct map where the motor domain densities appear at lower resolution, even near the MT surface, and a density appearing to connect the β-tubulin C-terminal tail and the KIF1A K-loop is observed (Fig. 5b). We suspect this weakly MT-bound state is detected in the P305L mutant and not in MT-bound WT KIF1A, due to the much poorer binding of this mutant. We propose that the P305L mutation impairs the formation of the

strongly MT-bound state and thus increases the fraction of weakly to strongly attached motor domains in the MT images. The P305L-ADP dataset has the lowest level of kinesin decoration (~9%) of all datasets (Supplementary Table 1).

To investigate the structural basis of the effects of the P305L mutation on MT binding, we compared the mutant and WT KIF1A structures of the motor domain with the highest resolution in the vicinity of the mutated KIF1A residue P305 (Fig. 6). P305 is located at the MT-binding interface and is part of the highly conserved loop-12 motif, (PYRD/E), which forms a 3_{10} helix in many kinesins including KIF1A. It has been previously hypothesized that the P305L mutation impairs MT binding by altering the conformation of this helix[77]. While we found that the P305L mutation indeed produces conformational changes, the observed changes are much more subtle than predicted (Fig.6a-c). The structure of the 3_{10} helix remains unaltered and most of the changes occur toward the N-terminal side of the mutation. The most noticeable structural difference between the P305L mutant and WT KIF1A is in the configuration of F303. The side chain of the introduced leucine residue in the P305L mutant would clash with the side chain of F303 in the WT structure (Fig.6) and would therefore cause the reorientation of F303 in the mutant. This structural difference between mutant and WT KIF1A suggests the possibility of rescuing the functionality of the P305L mutant by introducing a residue at position 303 that would not clash with a leucine at position 305. To test this hypothesis, we determined the mobility parameters of a KIF1A F303V single mutant and a F303V/P305L double mutant (Fig. 6d-f). We replaced phenylalanine at position 303 with valine as a less bulky but still hydrophobic amino acid. A valine is also found in this position in some kinesin-3s (e.g., Unc-104). While we found that the F303V single mutant exhibited reduced velocities and run lengths compared to WT KIF1A, the double mutant F303V/P305L indeed exhibited an increased run length relative to the P305L mutant while its run

length was still shorter than the run length of the F303V single mutant, demonstrating a partial rescue of the processivity in the double mutant.

Discussion

The kinesin-3 motor KIF1A is a highly processive and fast MT plus-end-directed motor protein and is essential for the long-distance transport in neurons[3-5], but how it achieves its unique motility properties remained largely unclear. Furthermore, while the majority of the ~150 identified KAND mutations are located within the motor domain, high-resolution structures of MT-bound KIF1A did not exist, which not only limited our ability to decipher KIF1A's motility mechanism but also the ability to perform structure-guided screens for small-molecule drugs to treat KAND. Here, we solved the high-resolution structures of MT-bound dimeric KIF1A as a function of nucleotide states and determined the first high-resolution structure of a KAND-associated mutant, P305L. The improved spatial resolution achieved in the present work enabled us to visualize novel structural features that are key to KIF1A's motility mechanism. Our work revealed a novel open conformation of KIF1A's nucleotide-binding pocket, the conformation of KIF1A's K-loop in the KIF1A-MT complex, the structure of the KIF1A dimer in the two-heads-bound state and the structural changes induced in the motor domain by the KAND P305L mutation.

In the presence of ADP or in the Apo state, KIF1A shows a single MT-bound motor domain with the nucleotide-binding pocket significantly more open than previously reported in the crystal structure of free KIF1A-ADP[58,60]. Similar open conformations have also been observed in high-resolution structures of tubulin and MT-bound complexes of kinesins from different subfamilies[69,70,79,80]. Thus, the open conformation observed here in the KIF1A-MT complexes

reinforces the existence of a conserved mechanism across the kinesin superfamily to couple MT binding with product release.

In previous structural studies on KIF1A, the K-loop was mostly not resolved[58,62-64], and it was unclear whether the inability to resolve the K-loop was due to the loop's disorder or mobility, or just due to a lack of sufficient resolution in the cryo-EM studies, or a combination of both. The high-resolution structures of the KIF1A-MT complexes presented here reveal the complete polypeptide path of the K-loop, although at lower resolution than other regions of the structure. This suggests that an insufficient resolution was one of the reasons why previous cryo-EM studies couldn't resolve the K-loop. On the other hand, given the high-resolution of X-ray crystallography studies, the lack of a fully resolved K-loop in these structures indicates the existence of a truly disordered K-loop, at least when KIF1A is in solution and not bound to MTs. Our results therefore suggest that MT binding partially induces an ordering of the K-loop so that it can be resolved only when KIF1A is bound to MTs. This conformational change is analogous to the one observed in other kinesins where MT binding induces ordering of areas of the motor domain that form the MT interface[64,70,81,82].

We show that most of the K-loop and its lysine residues are far away from the MT surface and do not appear to be forming stable contacts with the MT. Yet, the K-loop's lysines are important for KIF1A motility. We show that replacing KIF1A's K-loop for loop-12 of the kinesin-3 motor, KIF14, which has only a single positively charged residue located close to the MT interface, results in a significant reduction of the run-length of the motor. This result is consistent with recent reports that show that KIF1A's K-loop and its positively-charged residues are essential for KIF1A's superprocessivity[74,75].

Our structural and functional insights indicate that the K-loop's impact on KIF1A's superprocessivity is mediated by spatially mobile electrostatic interactions between the K-loop and the MT and not by specific close-range residue-to-residue contacts as observed in other areas of the KIF1A-MT interface. One of our cryoEM maps also appear to show a connection between the K-loop and the β-tubulin C-terminal tail where the motor domain appears to be weakly bound to the MT in a mobile state. The existence of such a connection provides a structural basis for a highly dynamic MT-bound state where a single motor domain undergoes directionally biased one-dimensional diffusion along the MT lattice[83]. This MT-bound state was shown to depend on the K-loop and the tubulin C-terminal tails[72].

The structure of the KIF1A-MT complex also provides evidence that the two motor domains of the KIF1A dimer are coordinated to facilitate processive movement. In the presence of AMP-PNP, when both MT-bound heads have an AMP-PNP molecule bound to their nucleotide pockets, the motor domains assume different conformations, indicating distinct points of their ATPase cycles. The leading head is in the open conformation with an undocked backward oriented neck-linker while the trailing head is in the closed catalytically active conformation with a docked neck-linker. This structure suggests that the ATP-hydrolysis step by the leading head is paused until the trailing head detaches from the MT. We also found evidence that the closed conformation of the trailing head is stabilized when the leading head is strongly bound to the MT. These observations strongly indicate that KIF1A's two motor domains move in a coordinated manner. However, our conclusion contrasts a recently proposed model in which KIF1A's superprocessivity arises from a K-loop-dependent enhanced-MT affinity in the detachment-prone, single-head-bound state of the motor, rather than from a tight coordination between KIF1A's two motor domains[75]. This model was based in part on the assumption that the neck-linker of KIF1A is longer

than the one of kinesin-1[75,84]. However, our structures show that the KIF1A neck-linker is actually shorter than the neck-linker of kinesin-1 and other kinesins. This result in a tighter connection between both motor domains in the two-heads-bound state than is the case for the kinesin-3 motor, KIF14, which has a longer neck-linker (Fig. 4). Furthermore, our mutagenesis result shows that making the KIF1A neck-linker more similar to the neck-linker of kinesin-1 by replacing the proline in the KIF1A neck-linker that marks the start the coiled-coil helix by the equivalent residue in the neck-linker of kinesin-1, results in a significant decrease in run-length. Thus, our results suggest that both K-loop-enhanced MT interactions and coordination between both motor domains contribute to KIF1A's superprocessivity.

Finally, with our improved workflow, we were able to solve the first cryoEM structure of a KIF1A KAND mutant bound to MTs. The solved structures showed that the P305L mutation produces an unexpected structural change. Rather than altering the structure of a highly conserved area of loop-12 just C-terminal to the mutation and known to be important for kinesin-MT binding[77], the largest structural differences were found in the configuration of F303, a residue located N-terminal to the mutation site. This structural change is the cause for the impaired MT binding of the P305L mutant. We also found that the F303V mutation results in a reduced processivity, which highlights the importance of this residue for processive movement. Replacing the equivalent residue in loop-12 of kinesin-1 has also been shown to result in impaired MT binding[85]. Interestingly, the P305L F303V double mutant improved the processivity over the processivity of the P305L mutant, suggesting this area of loop-12 could be target for future pharmacological interventions.

Methods

Cryo-EM

Preparation of microtubules

Microtubules (MTs) were prepared from porcine brain tubulin (Cytoskeleton, Inc. CO). Tubulin lyophilized pellets were resuspended in BRB80 (80 mM K-PIPES, 1 mM $MgCl_2$, 1 mM EGTA, pH 6.8) to 5 mg/mL and spun at 313,000 × *g* before polymerization to eliminate aggregates. MT polymerization was done in conditions to enrich the number of MTs with 15 protofilaments[86] as follows. The clarified resuspended tubulin solution was supplemented with 2 mM GTP, 4 mM $MgCl_2$, 12%(*v*/*v*) DMSO and incubated 40 minutes at 37 °C. An aliquot of stock Paclitaxel (Taxol®) solution (2 mM in DMSO) was added for a final paclitaxel concentration of 250 µM and incubated for another 40 minutes at 37 °C. The MTs were then spun at 15,500 × *g*, 25 °C and the pellet resuspended in BRB80 with 20 µM paclitaxel.

Cryo-EM of KIF1A-MT complexes

Four µL of 6 µM MT solution in BRB80 plus 20 µM paclitaxel were layered onto (UltrAuFoil R1.2/1.3 300 mesh) plasma cleaned just before use (Gatan Solarus plasma cleaner, at 15 W for 6 seconds in a 75% argon/25% oxygen atmosphere), the MTs were incubated 1 minute at room temperature and then the excess liquid removed from the grid using a Whatman #1 paper. Four µL of a solution of KIF1A WT in BRB80 supplemented with 20 µM paclitaxel (kinesin concentrations given in Supplementary Table 1) and either (1) 4 mM AMP-PNP, (2) 4 mM ADP, or (3) 5×10^{-3} units per µL apyrase (APO condition) were then applied onto the EM grid and incubated for 1 minute at room temperature. The grid was mounted into a Vitrobot apparatus (FEI-

ThermoFisher MA), incubated 1 minute at room temperature and plunge frozen into liquid ethane (Vitrobot settings: 100% humidity, 3 seconds blotting with Whatman #1 paper and 0 mm offset). Grids were stored in liquid nitrogen. For the P305L mutant, the kinesin solution was prepared as the solution for WT KIF1A with the difference that instead of BRB80 we used BRB36 (36 mM K-PIPES, 1 mM $MgCl_2$, 1 mM EGTA, pH 6.8) (Supplementary Table 1).

Cryo-EM data collection

Data were collected at 300 kV on Titan Krios microscopes equipped with a K3 summit detector. Acquisition was controlled using Leginon[87] with the image-shift protocol and partial correction for coma induced by beam tilt[88]. The pixel sizes, defocus ranges and cumulated dose are given in Table 1.

Processing of the cryo-EM datasets of MT-kinesin complexes

The processing was done similar as previously described[70]. Movie frames were aligned with Relion generating both dose-weighted and non-dose-weighted sums. Contrast transfer function (CTF) parameters per micrographs were estimated with Gctf[89] on aligned and non-dose-weighted movie averages.

Helical reconstruction on 15R MTs was performed using a helical-single-particle 3D analysis workflow in Frealign[90], as described previously[70,80] with 664 pixels box size, with each filament contributing only to one of the two half dataset. Per-particle CTF refinement was performed with FrealignX[91].

To select for tubulins bound to kinesin motors and to improve the resolution of the kinesin-tubulin complexes, the procedure HSARC[70] was used for these one-head-bound states. The procedure follows these steps:

(1) Relion helical refinement. The two independent Frealign helical refined half datasets were subjected to a single helical refinement in Relion 3.1[92] where each dataset was assigned to a distinct half-set and using as priors the Euler angle values determined in the helical-single-particle 3D reconstruction (initial resolution: 8 Å, sigma on Euler angles sigma_ang: 1.5, no helical parameter search).

(2) Asymmetric refinement with partial signal subtraction. Atomic models of kinesin-tubulin complexes derived from our recent work on KIF14[70] were used to generate a soft mask $mask_{full}$ using EMAN pdb2mrc and relion_mask_create (low-pass filtration: 30 Å, initial threshold: 0.05, extension: 14 pixels, soft edge: 8 pixels). For the one-head-bound only datasets (MT-KIF1A-ADP, MT-KIF1A-APO, MT-KIF1A^{P305L}-ADP and MT-KIF1A^{P305L}-APO), $mask_{full}$ was generated with a model containing 1 kinesin motor bound to 1 tubulin dimer and two longitudinally flanking tubulin subunits. For the datasets containing two-heads-bound states (MT-KIF1A-ANP and MT-KIF1A^{P305L}-ANP), $mask_{full}$ was generated from a kinesin dimer model bound to two tubulin dimers.

The helical dataset alignment file was symmetry expanded using the 15R MT symmetry of the dataset. Partial signal subtraction was then performed using $mask_{full}$ to retain the signal within that mask. During this procedure, images were re-centered on the projections of 3D coordinates of the center of mass of $mask_{full}$ (C_M) using a 416 pixels box size. The partially signal subtracted dataset was then used in a Relion 3D refinement procedure using as priors the Euler angle values determined form the Relion helical

refinement and the symmetry expansion procedure (initial resolution: 8 Å, sigma_ang: 5, offset range corresponding to 5 Å, healpix_order and auto_local_healpix_order set to 5). The CTF of each particle was corrected to account for their different position along the optical axis.

(3) 3D classification of the kinesin signal. A mask $mask_{kinesin}$ was generated like in step (2) but using only the kinesin coordinates (a single kinesin head for the datasets MT-KIF1A-ADP, MT-KIF1A-APO, MT-KIF1A^{P305L}-ADP and MT-KIF1A^{P305L}-APO ; a two-heads-bound kinesin dimer for the dataset MT-KIF1A-ANP and MT-KIF1A^{P305L}-ANP). A second partial signal subtraction procedure identical to first one in step (2) but using $mask_{kinesin}$ instead of $mask_{full,}$ with particles re-centered on the projections of C_M was performed to subtract all but the kinesin signal. The images obtained were resampled to 3.5 Å/pixel in 100-pixel boxes and the 3D refinement from step 2 was used to update the Euler angles and shifts of all particles.

For the datasets MT-KIF1A-ADP, MT-KIF1A-APO, MT-KIF1A^{P305L}-ADP and MT-KIF1A^{P305L}-APO with a single-head-bound state, a 3D focused classification without images alignment and using a mask for the kinesin generated like $mask_{kinesin}$ (low-pass filtration: 30 Å, initial threshold: 0.9, extension: 1 pixel, soft edge: 3 pixels) was then performed on the resampled dataset (8 classes, tau2_fudge: 4, padding: 2, iterations: 175). The class(es) showing a kinesin were selected and merged for the next step. For the MT-KIF1A^{P305L}-ADP which had very low decoration (~9 %, Supplementary Table 1), the previous classification led to a single decorated class (14% of the dataset) with a weak kinesin signal. Particles from this class were further classified in a second 3D classification (4 classes, tau2_fudge: 4, padding: 2, iterations: 175) and the main decorated class (68%)

with a recognizable kinesin was selected while the others (with resolution lower than 15 Å) were not.

For the MT-KIF1A-ANP and MT-KIF1A^{P305L}-ANP datasets, 3D classifications in 8 classes performed as described above on the partially subtracted data with 2 kinesin motor domains left revealed that both one-head- and two-heads-bound-states were present but not fully separated. The following hierarchical 3D-classification was used instead (Supplementary Figure 2, 3 and 4). Two different masks were generated (Supplementary Figure 2a-c): one covering the kinesin site closest to the (-) end of the MT called mask$_T$, and the other covering the kinesin site closest to the (+) end of the MT, called mask$_L$. These two masks cover respectively the trailing head and leading head of a two-heads-bound kinesin dimer bound to these two sites (sites T and L respectively, Supplementary Figure 2a-c). Each of these two masks was generated from an atomic model corresponding to the overlay of a trailing head and a leading head of a two-heads-bound kinesin dimer with its associated coiled-coil, so that the focused classification includes the signal of the coiled-coil independent of the kinesin registration (Supplementary Figure 2d-e). These models were converted to maps with EMAN pdb2mrc and the masks were generated with relion_mask_create (low-pass filtration: 30 Å, initial threshold: 1.3, extension: 1 pixel, soft edge: 3 pixels). First a 3D classification was performed focusing the classification on mask$_T$ (8 classes, tau2_fudge: 6, padding: 2, iterations: 175, Supplementary Figure 2f). Then a second focused classification using mask$_L$ (4 classes, tau2_fudge: 6, padding: 2, iterations: 175) was performed on the classes obtained in the previous classification step and selecting only the classes that were potentially trailing heads of a two-heads-bound state (Supplementary Figure 2f). This excluded classes that contained clear neck-linker and

coiled-coil cryo-EM densities toward the (-) end of the motor-domain density (i.e. a leading head), the classes that show no kinesin density and the classes having an unrecognizable signal. Each of the main classes used was named as indicated in Supplementary Figure 2f. The decoration and propensity of the states identified resulting from these classifications are given in Supplementary Table 1. All datasets produced at least one class where the kinesin motor densities were well-resolved.

(4) 3D reconstructions with original images (not signal subtracted). To avoid potential artifacts introduced by the signal subtraction procedure, final 3D reconstructions of each half dataset were obtained using relion_reconstruct on the original image-particles extracted from the micrographs without signal subtraction. To increase the resolution on the site T for the datasets MT-KIF1A-ANP and MT-KIF1A^{P305L}-ANP, some reconstructions were generated by merging the data from different classes obtained in the classification on the site T or L. In this case, the names of the classes are concatenated, for example, MT-KIF1A-ANP-$T_{23}L_1$ was generated by merging the data from MT-KIF1A-ANP-T_2L_1 and MT-KIF1A-ANP-T_3L_1.

(5) To obtain a final locally filtered and locally sharpened map for the states listed in table 1 (MT-KIF1A-ANP-$T_{23}L_1$, MT-KIF1A-ANP-T_2L_1, MT-KIF1A-ANP-T_3L_1, MT-KIF1A-ANP-T_1L_{02*}, MT-KIF1A-ADP, MT-KIF1A-APO, MT-KIF1A-ANP^{P305L}-TL_1, MT-KIF1A-ANP^{P305L}-TL_{012*}, MT-KIF1A-ADP, MT-KIF1A-APO), post-processing of the pair of unfiltered and unsharpened half maps was performed as follows. One of the two unfiltered half-map was low-pass-filtered to 15 Å and the minimal threshold value that does not show noise around the MT fragment was used to generate a mask with relion_mask_create (low-pass filtration: 15 Å, extension: 10 pixels, soft edge: 10 pixels). This soft mask was used

in blocres[93] on 12-pixel size boxes to obtain initial local resolution estimates. The merged map was locally filtered by blocfilt[93] using blocres local resolution estimates and then used for local low-pass filtration and local sharpening in localdeblur[94] with resolution search up to 25 Å. The localdeblur program converged to a filtration appropriate for the tubulin part of the map but over-sharpened for the kinesin part. The maps at every localdeblur cycle were saved and the map with better filtration for the kinesin part area was selected with the aim to improve the resolution of the kinesin loops.

The final reconstructions of MT-KIF1A-ANP-T_1L_1, MT-KIF1A-ANP-T_1L_0, MT-KIF1A-ANP-T_2L_0, MT-KIF1A-ANP-T_3L_0, MT-KIF1A-ANP-T_1L_*, MT-KIF1A-ANP-T_2L_*, MT-KIF1A-ANP-T_3L_* (Supplementary Fig.3) were low-passed filtered at 4.0 Å and sharpened with a b-factor of -40 A^2.

Cryo-EM resolution estimation

The final resolutions for each cryo-EM class average reconstruction listed in table 1 (MT-KIF1A-ANP-$T_{23}L_1$, MT-KIF1A-ANP-T_2L_1, MT-KIF1A-ANP-T_3L_1, MT-KIF1A-ANP-T_1L_{02*}, MT-KIF1A-ADP, MT-KIF1A-APO, MT-KIF1A-ANP^{P305L}-TL_1, MT-KIF1A-ANP^{P305L}-TL_{012*}, MT-KIF1A-ADP, MT-KIF1A-APO) were estimated from FSC curves generated with Relion 3.1 postprocess ($FSC_{0.143}$ criteria, Supplementary Figure 5). To estimate the overall resolution, these curves were computed from the two independently refined half maps (gold standard) using soft masks that isolate a single asymmetric unit containing a kinesin and a tubulin dimer. The soft masks were created with Relion 3.1 relion_mask_create (for MT datasets: low pass filtration: 15 Å, threshold: 0.1, extension: 2 pixels, soft edge: 5 pixels) applied on the correctly positioned EMAN pdb2mrc density map generated with the coordinates of the respective refined atomic models. FSC

curves for the tubulin or kinesin parts of the maps were generated similarly using the corresponding subset of the PDB model to mask only a kinesin or a tubulin dimer (Supplementary Fig. 5, Table 1).

The final cryo-EM maps together with the corresponding half maps, the masks used for resolution estimation, the masks used in the partial signal subtraction for the MT datasets, and the FSC curves are deposited in the Electron Microscopy Data Bank (Table 1).

Model building

Atomic models of the cryo-EM density maps were built as follow. First, atomic models for each protein chains were generated from their amino-acid sequence by homology modeling using Modeller[95]. Second, the protein chains were manually placed into the cryo-EM densities and fitted as rigid bodies using UCSF-Chimera[96]. Third, the models were flexibly fitted into the density maps using Rosetta for cryo-EM relax protocols[97,98] and the models with the best scores (best match to the cryo-EM density and best molprobity scores) were selected. Fourth, the Rosetta-refined models were further refined against the cryo-EM density maps using Phenix real space refinement tools[99]. Fifth, the Phenix-refined models were edited using Coot[100]. Several iterations of Phenix real space refinement and Coot editing were performed to reach the final atomic models.

Atomic models and cryo-EM map figures were prepared with UCSF-Chimera[96] or USCF ChimeraX[101] and R[102].

Generation of plasmids for KIF1A constructs

A plasmid for a previous published KIF1A construct[9] (KIF1A(Homo sapiens, aa 1-393)-leucine zipper-SNAPf-EGFP-6His) was used as the template for all constructs in this study. For proteins used in the cryo-EM studies, the SNAPf-EGFP-6His tag was replaced with a strep-II tag (IBA Lifesciences GmbH) using Q5 mutagenesis (New England Biolabs Inc., #E0554S). Mutations within KIF1A were generated using Q5 mutagenesis. All plasmids were confirmed by sequencing.

Protein expression in *E. coli*

KIF1A expression was performed as described in previous studies[9,52]. Briefly, each plasmid was transformed into BL21-CodonPlus(DE3)-RIPL competent cells (Agilent Technologies, #230280). A single colony was picked and inoculated in 1 mL of terrific broth (TB) (protocol adopted from Cold Spring Harbor protocol, DOI: 10.1101/pdb.rec8620) with 50 µg/mL carbenicillin and 50 µg/mL chloramphenicol. The 1-mL culture was shaken at 37 °C overnight, and then inoculated into 400 mL of TB (or 1–2 L for cryo-EM studies) with 2 µg/mL carbenicillin and 2 µg/mL chloramphenicol. The culture was shaken at 37 °C for 5 hours and then cooled on ice for 1 hour. IPTG was then added to the culture to a final concentration of 0.1 mM to induce expression. Afterwards, the culture was shaken at 16 °C overnight. The cells were harvested by centrifugation at 3,000 rcf for 10 minutes at 4°C. The supernatant was discarded, and 1.25 mL of B-PER™ Complete Bacterial Protein Extraction Reagent (ThermoFisher Scientific, #89821) per 100 mL culture with 2 mM $MgCl_2$, 1 mM EGTA, 1 mM DTT, 0.1 mM ATP, and 2 mM PMSF was added to the cell pellet. The cells were fully resuspended and flash frozen in liquid nitrogen. If the purification was not done on the same day, the frozen cells were stored at –80 °C.

Protein purification

To purify the protein, the frozen cell pellet was thawed at 37 °C. The solution was nutated at room temperature for 20 minutes and then dounced for 10 strokes on ice to lyse the cells. Unless specified, the following procedures were done at 4 °C. The cell lysate was cleared by centrifugation at 80,000 rpm (260,000 rcf, *k*-factor=28) for 10 minutes in an TLA-110 rotor using a Beckman Tabletop Ultracentrifuge Unit. The supernatant was flown through 500 μL of Roche cOmplete™ His-Tag purification resin (Millipore Sigma, #5893682001) for His-tag tagged proteins, or 2 mL of Strep-Tactin® Sepharose® resin (IBA Lifesciences GmbH, #2-1201-002) for strep-II tagged proteins. The resin was washed with wash buffer (WB) (for His-tagged protein: 50 mM HEPES, 300 mM KCl, 2 mM $MgCl_2$, 1 mM EGTA, 1 mM DTT, 1 mM PMSF, 0.1 mM ATP, 0.1% Pluronic F-127 (w/v), 10% glycerol, pH 7.2; for strep-II tagged protein, Pluronic F-127 and glycerol were omitted). For proteins with a SNAPf-tag, the resin was mixed with 10 μM SNAP-Cell® TMR-Star (New England Biolabs Inc., #S9105S) at room temperature for 10 minutes to label the SNAPf-tag. The resin was further washed with WB, and then eluted with elution buffer (EB) (for His-tagged protein: 50 mM HEPES, 150 mM KCl, 150 mM imidazole, 2 mM $MgCl_2$, 1 mM EGTA, 1 mM DTT, 1 mM PMSF, 0.1 mM ATP, 0.1% Pluronic F-127 (w/v), 10% glycerol, pH 7.2; for strep-II tagged protein: 80 mM PIPES, 2 mM $MgCl_2$, 1 mM EGTA, 1 mM DTT, 0.1 mM ATP, 5 mM desthiobiotin). The Ni-NTA elute was flash frozen and stored at –80 °C. The Strep-Tactin elute was concentrated using a Amicon Ultra-0.5 mL Centrifugal Filter Unit (30-kDa MWCO) (Millipore Sigma, #UFC503024). Storage buffer (SB) (80 mM PIPES, 2 mM $MgCl_2$, 80% sucrose (w/v) was added to the protein solution to have a final 20% sucrose (w/v) concentration, and the

protein solution was flash frozen and stored at -80 °C. The purity of the proteins was confirmed on polyacrylamide gels.

Microtubule-binding and -release assay

An MT-binding and -release (MTBR) assay was performed to remove inactive motors for single-molecule TIRF assay. 50 µL of eluted protein was buffer-exchanged into a low salt buffer (30 mM HEPES, 50 mM KCl, 2 mM $MgCl_2$, 1 mM EGTA, 1 mM DTT, 1 mM AMP-PNP, 10 µM taxol, 0.1% Pluronic F-127 (w/v), and 10% glycerol) using 0.5-mL Zeba™ spin desalting column (7-kDa MWCO) (ThermoFisher Scientific, #89882). The solution was warmed to room temperature and 5 µL of 5 mg/mL taxol-stabilized MTs was added. The solution was well mixed and incubated at room temperature for 2 minutes to allow motors to bind to the MTs and then spun through a 100 µL glycerol cushion (80 mM PIPES, 2 mM $MgCl_2$, 1 mM EGTA, 1 mM DTT, 10 µM taxol, and 60% glycerol, pH 6.8) by centrifugation at 45,000 rpm (80,000 rcf, *k*-factor=33) for 10 minutes at room temperature in TLA-100 rotor using a Beckman Tabletop Ultracentrifuge Unit. Next, the supernatant was removed and the pellet was resuspended in 50 µL high salt release buffer (30 mM HEPES, 300 mM KCl, 2 mM $MgCl_2$, 1 mM EGTA, 1 mM DTT, 10 µM taxol, 3 mM ATP, 0.1% Pluronic F-127 (w/v), and 10% glycerol). The MTs were then removed by centrifugation at 40,000 rpm (60,000 rcf, *k*-factor=41) for 5 minutes at room temperature. Finally, the supernatant containing the active motors was aliquoted, flash frozen in liquid nitrogen, and stored at –80 °C.

Single-molecule TIRF motility assay

MTBR fractions were used for the single-molecule TIRF assay and the dilutions were adjusted to an appropriate density of motors on MTs. The assay was performed as described before[103] except the motility buffer was BRB80 (80 mM PIPES, 2 mM $MgCl_2$, 1 mM EGTA, 1 mM DTT, 10 µM taxol, 0.5% Pluronic F-127 (w/v), 2 mM ATP, 5 mg/mL BSA, 1 mg/mL α-casein, gloxy oxygen scavenging system, and 10% glycerol, pH 6.8). Images were acquired with 200 ms per frame (total 600 frames per movie), and then analyzed via a custom-written MATLAB software. Kymographs were generated using ImageJ2 (version 2.9.0). Statistical analysis was performed and graphs were generated using GraphPad Prism (version 9.5.0).

Acknowledgements

This work was supported by National Institutes of Health Grant R01GM113164 (H.S.), R01GM098469 (AG) and R01NS114636(A.G.). Cryo-EM data collection was performed at the Simons Electron Microscopy Center and National Resource for Automated Molecular Microscopy located at the New York Structural Biology Center, supported by grants from the Simons Foundation (SF349247), NYSTAR, and the NIH National Institute of General Medical Sciences (GM103310) with additional support from Agouron Institute (F00316) and NIH (OD019994).

Author contributions

L.R. generated, expressed, and purified the constructs for the cryo-EM and single-molecule studies. L.R. performed single-molecule experiments, collected and analyzed the data, and interpreted the results. M.P.M.H.B. and A.B.A. assembled kinesin-MT complexes and made cryo-EM grid samples; A.B.A. performed sample screening and optimization for cryo-EM imaging and performed MT selection; M.P.M.H.B., A.B.A. and H.S. designed the cryo-EM experiments; M.P.M.H.B. and A.B.A. performed cryo-EM data collection; M.P.M.H.B. designed and performed the cryo-EM data processing of kinesin-MT complexes and interpreted the results ; M.P.M.H.B. and H.S. built and refined the atomic models, and interpreted the structures; A.G. and H.S. conceived and coordinated the project and interpreted the results; M.P.M.H.B., L.R, A.B.A., A.G., and H.S. wrote the manuscript.

References

1. Carabalona, A., Hu, D.J. & Vallee, R.B. KIF1A inhibition immortalizes brain stem cells but blocks BDNF-mediated neuronal migration. *Nat Neurosci* **19**, 253-62 (2016).
2. Tsai, J.-W., Lian, W.-N., Kemal, S., Kriegstein, A.R. & Vallee, R.B. Kinesin 3 and cytoplasmic dynein mediate interkinetic nuclear migration in neural stem cells. *Nat Neurosci* **13**, 1463-1471 (2010).
3. Barkus, R.V., Klyachko, O., Horiuchi, D., Dickson, B.J. & Saxton, W.M. Identification of an axonal kinesin-3 motor for fast anterograde vesicle transport that facilitates retrograde transport of neuropeptides. *Mol. Biol. Cell* **19**, 274-283 (2008).
4. Hall, D.H. & Hedgecock, E.M. Kinesin-related gene unc-104 is required for axonal transport of synaptic vesicles in C. elegans. *Cell* **65**, 837-47 (1991).
5. Lo, K.Y., Kuzmin, A., Unger, S.M., Petersen, J.D. & Silverman, M.A. KIF1A is the primary anterograde motor protein required for the axonal transport of dense-core vesicles in cultured hippocampal neurons. *Neurosci Lett* **491**, 168-73 (2011).
6. Okada, Y., Yamazaki, H., Sekine-Aizawa, Y. & Hirokawa, N. The neuron-specific kinesin superfamily protein KIF1A is a unique monomeric motor for anterograde axonal transport of synaptic vesicle precursors. *Cell* **81**, 769-80 (1995).
7. Yonekawa, Y. et al. Defect in synaptic vesicle precursor transport and neuronal cell death in KIF1A motor protein-deficient mice. *J Cell Biol* **141**, 431-441 (1998).
8. Zahn, T.R. et al. Dense core vesicle dynamics in Caenorhabditis elegans neurons and the role of kinesin UNC-104. *Traffic* **5**, 544-559 (2004).
9. Boyle, L. et al. Genotype and defects in microtubule-based motility correlate with clinical severity in KIF1A Associated Neurological Disorder. *Human Genetics and Genomics Advances* **2**(2021).
10. Gabrych, D.R., Lau, V.Z., Niwa, S. & Silverman, M.A. Going Too Far Is the Same as Falling Short(dagger): Kinesin-3 Family Members in Hereditary Spastic Paraplegia. *Front Cell Neurosci* **13**, 419 (2019).
11. Guo, Y. et al. A Rare KIF1A Missense Mutation Enhances Synaptic Function and Increases Seizure Activity. *Front Genet* **11**, 61 (2020).
12. John, A., Ng-Cordell, E., Hanna, N., Brkic, D. & Baker, K. The neurodevelopmental spectrum of synaptic vesicle cycling disorders. *J Neurochem* **157**, 208-228 (2020).
13. Nicita, F. et al. Heterozygous KIF1A variants underlie a wide spectrum of neurodevelopmental and neurodegenerative disorders. *J Med Genet* **58**, 475-483 (2020).
14. Van Beusichem, A.E. et al. Mobility Characteristics of Children with Spastic Paraplegia Due to a Mutation in the KIF1A Gene. *Neuropediatrics* **51**, 146-153 (2020).
15. Riviere, J.B. et al. KIF1A, an axonal transporter of synaptic vesicles, is mutated in hereditary sensory and autonomic neuropathy type 2. *Am J Hum Genet* **89**, 219-30 (2011).
16. Erlich, Y. et al. Exome sequencing and disease-network analysis of a single family implicate a mutation in KIF1A in hereditary spastic paraparesis. *Genome Res* **21**, 658-64 (2011).
17. Hamdan, F.F. et al. Excess of de novo deleterious mutations in genes associated with glutamatergic systems in nonsyndromic intellectual disability. *Am J Hum Genet* **88**, 306-16 (2011).

18. Klebe, S. et al. KIF1A missense mutations in SPG30, an autosomal recessive spastic paraplegia: distinct phenotypes according to the nature of the mutations. *Eur J Hum Genet* **20**, 645-9 (2012).
19. Okamoto, N. et al. KIF1A mutation in a patient with progressive neurodegeneration. *J Hum Genet* **59**, 639-41 (2014).
20. Jamuar, S.S. & Walsh, C.A. Somatic mutations in cerebral cortical malformations. *N Engl J Med* **371**, 2038 (2014).
21. Lee, J.R. et al. De novo mutations in the motor domain of KIF1A cause cognitive impairment, spastic paraparesis, axonal neuropathy, and cerebellar atrophy. *Hum Mutat* **36**, 69-78 (2015).
22. Esmaeeli Nieh, S. et al. De novo mutations in KIF1A cause progressive encephalopathy and brain atrophy. *Ann Clin Transl Neurol* **2**, 623-35 (2015).
23. Ylikallio, E. et al. Dominant transmission of de novo KIF1A motor domain variant underlying pure spastic paraplegia. *Eur J Hum Genet* **23**, 1427-30 (2015).
24. Citterio, A. et al. Variants in KIF1A gene in dominant and sporadic forms of hereditary spastic paraparesis. *J Neurol* **262**, 2684-90 (2015).
25. Ohba, C. et al. De novo KIF1A mutations cause intellectual deficit, cerebellar atrophy, lower limb spasticity and visual disturbance. *J Hum Genet* **60**, 739-42 (2015).
26. Megahed, H. et al. Utility of whole exome sequencing for the early diagnosis of pediatric-onset cerebellar atrophy associated with developmental delay in an inbred population. *Orphanet J Rare Dis* **11**, 57 (2016).
27. Hotchkiss, L. et al. Novel De Novo Mutations in KIF1A as a Cause of Hereditary Spastic Paraplegia With Progressive Central Nervous System Involvement. *J Child Neurol* **31**, 1114-9 (2016).
28. Iqbal, Z. et al. Targeted high throughput sequencing in hereditary ataxia and spastic paraplegia. *PLoS One* **12**, e0174667 (2017).
29. Hasegawa, A. et al. Co-existence of spastic paraplegia-30 with novel KIF1A mutation and spinocerebellar ataxia 31 with intronic expansion of BEAN and TK2 in a family. *J Neurol Sci* **372**, 128-130 (2017).
30. Krenn, M. et al. Hereditary spastic paraplegia caused by compound heterozygous mutations outside the motor domain of the KIF1A gene. *Eur J Neurol* **24**, 741-747 (2017).
31. Cheon, C.K. et al. Autosomal dominant transmission of complicated hereditary spastic paraplegia due to a dominant negative mutation of KIF1A, SPG30 gene. *Sci Rep* **7**, 12527 (2017).
32. Roda, R.H., Schindler, A.B. & Blackstone, C. Multigeneration family with dominant SPG30 hereditary spastic paraplegia. *Ann Clin Transl Neurol* **4**, 821-824 (2017).
33. Travaglini, L. et al. The impact of next-generation sequencing on the diagnosis of pediatric-onset hereditary spastic paraplegias: new genotype-phenotype correlations for rare HSP-related genes. *Neurogenetics* **19**, 111-121 (2018).
34. Demily, C. et al. Additive Effect of Variably Penetrant 22q11.2 Duplication and Pathogenic Mutations in Autism Spectrum Disorder: To Which Extent Does the Tree Hide the Forest? *J Autism Dev Disord* **48**, 2886-2889 (2018).
35. Dong, F., Costigan, D.C. & Howitt, B.E. Targeted next-generation sequencing in the detection of mismatch repair deficiency in endometrial cancers. *Mod Pathol* **32**, 252-257 (2019).

36. Samanta, D. & Gokden, M. PEHO syndrome: KIF1A mutation and decreased activity of mitochondrial respiratory chain complex. *J Clin Neurosci* **61**, 298-301 (2019).
37. Tomaselli, P.J. et al. A de novo dominant mutation in KIF1A associated with axonal neuropathy, spasticity and autism spectrum disorder. *J Peripher Nerv Syst* **22**, 460-463 (2017).
38. Yoshikawa, K. et al. The novel de novo mutation of KIF1A gene as the cause for Spastic paraplegia 30 in a Japanese case. *eNeurologicalSci* **14**, 34-37 (2019).
39. Volk, A., Conboy, E., Wical, B., Patterson, M. & Kirmani, S. Whole-Exome Sequencing in the Clinic: Lessons from Six Consecutive Cases from the Clinician's Perspective. *Mol Syndromol* **6**, 23-31 (2015).
40. Sun, M. et al. Targeted exome analysis identifies the genetic basis of disease in over 50% of patients with a wide range of ataxia-related phenotypes. *Genet Med* **21**, 195-206 (2019).
41. Muir, A.M. et al. Genetic heterogeneity in infantile spasms. *Epilepsy Res* **156**, 106181 (2019).
42. Kashimada, A. et al. Genetic analysis of undiagnosed ataxia-telangiectasia-like disorders. *Brain Dev* **41**, 150-157 (2019).
43. Pennings, M. et al. KIF1A variants are a frequent cause of autosomal dominant hereditary spastic paraplegia. *Eur J Hum Genet* **28**, 40-49 (2020).
44. Xiaojing, W. et al. Generation of a human induced pluripotent stem cell line (SDUBMSi001-A) from a hereditary spastic paraplegia patient carrying kif1a c.773C>T missense mutation. *Stem Cell Res* **43**, 101727 (2020).
45. van de Warrenburg, B.P. et al. Clinical exome sequencing for cerebellar ataxia and spastic paraplegia uncovers novel gene-disease associations and unanticipated rare disorders. *Eur J Hum Genet* **24**, 1460-6 (2016).
46. Raffa, L. et al. Optic nerve hypoplasia in a patient with a de novo KIF1A heterozygous mutation. *Can J Ophthalmol* **52**, e169-e171 (2017).
47. Hosokawa, S., Kubo, Y., Arakawa, R., Takashima, H. & Saito, K. Analysis of spinal muscular atrophy-like patients by targeted resequencing. *Brain Dev* **42**, 148-156 (2020).
48. Spagnoli, C., Rizzi, S., Salerno, G.G., Frattini, D. & Fusco, C. Long-term follow-up until early adulthood in autosomal dominant, complex SPG30 with a novel KIF1A variant: a case report. *Ital J Pediatr* **45**, 155 (2019).
49. Kurihara, M. et al. A Novel de novo KIF1A Mutation in a Patient with Autism, Hyperactivity, Epilepsy, Sensory Disturbance, and Spastic Paraplegia. *Intern Med* **59**, 839-842 (2020).
50. Nemani, T. et al. KIF1A-related disorders in children: A wide spectrum of central and peripheral nervous system involvement. *J Peripher Nerv Syst* **25**, 117-124 (2020).
51. Langlois, S. et al. De novo dominant variants affecting the motor domain of KIF1A are a cause of PEHO syndrome. *Eur J Hum Genet* **24**, 949-53 (2016).
52. Budaitis, B.G. et al. Pathogenic mutations in the kinesin-3 motor KIF1A diminish force generation and movement through allosteric mechanisms. *J Cell Biol* **220**(2021).
53. Guedes-Dias, P. et al. Kinesin-3 Responds to Local Microtubule Dynamics to Target Synaptic Cargo Delivery to the Presynapse. *Curr Biol* **29**, 268-282 e8 (2019).
54. Chiba, K. et al. Disease-associated mutations hyperactivate KIF1A motility and anterograde axonal transport of synaptic vesicle precursors. *Proc Natl Acad Sci U S A* **116**, 18429-18434 (2019).

55. Endow, S.A., Kull, F.J. & Liu, H. Kinesins at a glance. *J Cell Sci* **123**, 3420-4 (2010).
56. Miki, H., Setou, M., Kaneshiro, K. & Hirokawa, N. All kinesin superfamily protein, KIF, genes in mouse and human. *Proc Natl Acad Sci U S A* **98**, 7004-11 (2001).
57. Soppina, V. & Verhey, K.J. The family-specific K-loop influences the microtubule on-rate but not the superprocessivity of kinesin-3 motors. *Mol Biol Cell* **25**, 2161-70 (2014).
58. Kikkawa, M. et al. Switch-based mechanism of kinesin motors. *Nature* **411**, 439-445 (2001).
59. Nitta, R., Kikkawa, M., Okada, Y. & Hirokawa, N. KIF1A alternately uses two loops to bind microtubules. *Science* **305**, 678-683 (2004).
60. Nitta, R., Okada, Y. & Hirokawa, N. Structural model for strain-dependent microtubule activation of Mg-ADP release from kinesin. in *Nat Struct Mol Biol* Vol. 15 1067-1075 (2008).
61. Morikawa, M. et al. A neuropathy-associated kinesin KIF1A mutation hyper-stabilizes the motor-neck interaction during the ATPase cycle. *EMBO J* **41**, e108899 (2022).
62. Kikkawa, M., Okada, Y. & Hirokawa, N. 15 A resolution model of the monomeric kinesin motor, KIF1A. *Cell* **100**, 241-252 (2000).
63. Kikkawa, M. & Hirokawa, N. High-resolution cryo-EM maps show the nucleotide binding pocket of KIF1A in open and closed conformations. *EMBO J* **25**, 4187-4194 (2006).
64. Atherton, J. et al. Conserved mechanisms of microtubule-stimulated ADP release, ATP binding, and force generation in transport kinesins. *Elife* **3**, e03680 (2014).
65. Subramaniam, S., Earl, L.A., Falconieri, V., Milne, J.L. & Egelman, E.H. Resolution advances in cryo-EM enable application to drug discovery. *Curr Opin Struct Biol* **41**, 194-202 (2016).
66. Ceska, T., Chung, C.W., Cooke, R., Phillips, C. & Williams, P.A. Cryo-EM in drug discovery. *Biochem Soc Trans* **47**, 281-293 (2019).
67. Tomishige, M., Klopfenstein, D.R. & Vale, R.D. Conversion of Unc104/KIF1A kinesin into a processive motor after dimerization. *Science* **297**, 2263-2267 (2002).
68. Klopfenstein, D.R., Tomishige, M., Stuurman, N. & Vale, R.D. Role of phosphatidylinositol(4,5)bisphosphate organization in membrane transport by the Unc104 kinesin motor. *Cell* **109**, 347-358 (2002).
69. Hunter, B. et al. Kinesin-8-specific loop-2 controls the dual activities of the motor domain according to tubulin protofilament shape. *Nat Commun* **13**, 4198 (2022).
70. Benoit, M. et al. Structural basis of mechano-chemical coupling by the mitotic kinesin KIF14. *Nat Commun* **12**, 3637 (2021).
71. Cross, R.A. Review: Mechanochemistry of the kinesin-1 ATPase. *Biopolymers* **105**, 476-82 (2016).
72. Okada, Y. & Hirokawa, N. Mechanism of the single-headed processivity: diffusional anchoring between the K-loop of kinesin and the C terminus of tubulin. in *Proc Natl Acad Sci USA* Vol. 97 640-645 (2000).
73. Lessard, D.V. et al. Polyglutamylation of tubulin's C-terminal tail controls pausing and motility of kinesin-3 family member KIF1A. *J Biol Chem* **294**, 6353-6363 (2019).
74. Pyrpassopoulos, S., Gicking, A.M., Zaniewski, T.M., Hancock, W.O. & Ostap, E.M. KIF1A is kinetically tuned to be a superengaging motor under hindering loads. *Proc Natl Acad Sci U S A* **120**, e2216903120 (2023).

75. Zaniewski, T.M. & Hancock, W.O. Positive charge in the K-loop of the kinesin-3 motor KIF1A regulates superprocessivity by enhancing microtubule affinity in the one-head-bound state. *J Biol Chem* **299**, 102818 (2022).
76. Shastry, S. & Hancock, W.O. Neck Linker Length Determines the Degree of Processivity in Kinesin-1 and Kinesin-2 Motors. *Curr Biol* **20**, 939-943 (2010).
77. Lam, A.J. et al. A highly conserved 310 helix within the kinesin motor domain is critical for kinesin function and human health. *Sci Adv* **7**(2021).
78. Sindelar, C.V. & Downing, K.H. The beginning of kinesin's force-generating cycle visualized at 9-A resolution. *J Cell Biol* **177**, 377-85 (2007).
79. Cao, L. et al. The structure of apo-kinesin bound to tubulin links the nucleotide cycle to movement. *Nat Commun* **5**, 5364 (2014).
80. Benoit, M., Asenjo, A.B. & Sosa, H. Cryo-EM reveals the structural basis of microtubule depolymerization by kinesin-13s. *Nat Commun* **9**, 1662 (2018).
81. Wang, W. et al. Kif2C minimal functional domain has unusual nucleotide binding properties that are adapted to microtubule depolymerization. *J Biol Chem* **287**, 15143-53 (2012).
82. Shang, Z. et al. High-resolution structures of kinesin on microtubules provide a basis for nucleotide-gated force-generation. *Elife* **3**, e04686 (2014).
83. Okada, Y. & Hirokawa, N. A processive single-headed motor: kinesin superfamily protein KIF1A. in *Science* Vol. 283 1152-1157 (1999).
84. Hariharan, V. & Hancock, W.O. Insights into the Mechanical Properties of the Kinesin Neck Linker Domain from Sequence Analysis and Molecular Dynamics Simulations. *Cell Mol Bioeng* **2**, 177-189 (2009).
85. Woehlke, G. et al. Microtubule Interaction Site of the Kinesin Motor. *Cell* **90**, 207-216 (1997).
86. Wilson-Kubalek, E.M., Cheeseman, I.M. & Milligan, R.A. Structural comparison of the Caenorhabditis elegans and human Ndc80 complexes bound to microtubules reveals distinct binding behavior. *Mol Biol Cell* **27**, 1197-203 (2016).
87. Suloway, C. et al. Automated molecular microscopy: the new Leginon system. *J Struct Biol* **151**, 41-60 (2005).
88. Glaeser, R.M., Typke, D., Tiemeijer, P.C., Pulokas, J. & Cheng, A. Precise beam-tilt alignment and collimation are required to minimize the phase error associated with coma in high-resolution cryo-EM. *J Struct Biol* **174**, 1-10 (2011).
89. Zhang, K. Gctf: Real-time CTF determination and correction. *J Struct Biol* **193**, 1-12 (2016).
90. Grigorieff, N. Frealign: An Exploratory Tool for Single-Particle Cryo-EM. *Methods Enzymol* **579**, 191-226 (2016).
91. Grant, T., Rohou, A. & Grigorieff, N. cisTEM, user-friendly software for single-particle image processing. *Elife* **7**(2018).
92. Zivanov, J. et al. New tools for automated high-resolution cryo-EM structure determination in RELION-3. *Elife* **7**(2018).
93. Heymann, J.B. & Belnap, D.M. Bsoft: image processing and molecular modeling for electron microscopy. *J Struct Biol* **157**, 3-18 (2007).
94. Ramirez-Aportela, E. et al. Automatic local resolution-based sharpening of cryo-EM maps. *Bioinformatics* **36**, 765-772 (2020).

95. Fiser, A. & Sali, A. Modeller: generation and refinement of homology-based protein structure models. *Methods Enzymol* **374**, 461-91 (2003).
96. Pettersen, E.F. et al. UCSF Chimera--a visualization system for exploratory research and analysis. *J Comput Chem* **25**, 1605-12 (2004).
97. DiMaio, F., Tyka, M.D., Baker, M.L., Chiu, W. & Baker, D. Refinement of protein structures into low-resolution density maps using rosetta. *J Mol Biol* **392**, 181-90 (2009).
98. Wang, R.Y. et al. De novo protein structure determination from near-atomic-resolution cryo-EM maps. *Nat Methods* **12**, 335-8 (2015).
99. Adams, P.D. et al. PHENIX: a comprehensive Python-based system for macromolecular structure solution. *Acta Crystallogr D Biol Crystallogr* **66**, 213-21 (2010).
100. Emsley, P. & Cowtan, K. Coot: model-building tools for molecular graphics. *Acta Crystallogr D Biol Crystallogr* **60**, 2126-32 (2004).
101. Goddard, T.D. et al. UCSF ChimeraX: Meeting modern challenges in visualization and analysis. *Protein Sci* **27**, 14-25 (2018).
102. Ihaka, R. & Gentleman, R.R. R: A Language for Data Analysis and Graphics. *J. Comput. Graph. Stat.* **5**, 299–314 (1996).
103. Rao, L. & Gennerich, A. Single-Molecule Studies on the Motion and Force Generation of the Kinesin-3 Motor KIF1A. *Methods Mol Biol* **2478**, 585-608 (2022).

Table 1. Cryo-EM data collection, refinement and validation statistics (1/3)

	MT-KIF1A-ANP-$T_{23}L_1$ (EMDB-xxxxx) (PDB xxxx)	**MT-KIF1A-ANP-T_2L_1** (EMDB-xxxxx) (PDB xxxx)	**MT-KIF1A-ANP-T_3L_1** (EMDB-xxxxx) (PDB xxxx)	**MT-KIF1A-ANP-T_1L_{02*}** (EMDB-xxxxx) (PDB xxxx)
Data collection and processing				
Magnification (actual)	59242	59242	59242	59242
Voltage (kV)	300	300	300	300
Electron exposure (e^-/Å^2)	50.2	50.2	50.2	50.2
Defocus range (μm) [a]	0.8 ; 1.7	0.8 ; 1.7	0.8 ; 1.7	0.8 ; 1.7
Pixel size (Å)	0.844	0.844	0.844	0.844
Symmetry imposed [b]	Helical	Helical	Helical	Helical
Rise (Å)	5.60	5.60	5.60	5.60
Twist (deg)	168.09	168.09	168.09	168.09
Particle images identified as 15R symmetry (no.)	60199	60199	60199	60199
Particle images in helical reconstruction (no.)	60199	60199	60199	60199
Single particles (no.) [c]	902985	902985	902985	902985
Single particles used (no.) [d]	117091	99325	89711	116194
Overall resolution (Å)	3.0	3.2	3.1	3.1
FSC threshold	0.143	0.143	0.143	0.143
Kinesin resolution (Å)	3.2	3.4	3.3	3.3
Tubulin resolution (Å)	2.9	3.1	3.1	3.0
Refinement				
Model composition				
Non-hydrogen atoms	20067	20067	20067	16860
Protein residues	2518	2518	2518	2114
Ligands	11	11	11	10
R.m.s. deviations				
Bond lengths (Å)	0.0053	0.0053	0.0055	0.0054
Bond angles (°)	1.14	1.13	1.14	1.15
Validation				
MolProbity score	1.24	1.08	1.08	1.57
Clashscore	3.04	2.40	2.20	4.83
Poor rotamers (%)	1.06	0.09	0.32	1.54
Ramachandran plot				
Favored (%)	97.36	97.72	97.60	96.99
Allowed (%)	2.56	2.16	2.28	2.72
Disallowed (%)	0.08	0.12	0.12	0.29

[a] Range of the per-particle defocus estimates. The range corresponds to 90% of the particles used, 5% of the particle defocuses are below and 5% are above this range.
[b] Symmetry imposed during the symmetrical refinement done before the local refinements (rise and twists provided for helical symmetry only).
[c] Total number of particles after symmetry expansion.
[d] Number of asymmetric units, corresponding to a kinesin motor bound to a tubulin dimer, used after 3D classification.

Table 1. Cryo-EM data collection, refinement and validation statistics (2/3)

	MT-KIF1A-ADP (EMDB-xxxxx) (PDB xxxx)	**MT-KIF1A-APO** (EMDB-xxxxx) (PDB xxxx)	**MT-KIF1A^{P305L}-ANP-TL$_1$** (EMDB-xxxxx) (PDB xxxx)
Data collection and processing			
Magnification (actual)	59242	57078	59242
Voltage (kV)	300	300	300
Electron exposure (e^-/Å^2)	67.5	62.9	49.4
Defocus range (μm) [a]	0.9 ; 2.1	0.7 ; 1.7	1.0. ; 2.4
Pixel size (Å)	0.844	0.876	0.844
Symmetry imposed [b]	Helical	Helical	Helical
Rise (Å)	5.61	5.61	5.64
Twist (deg)	168.09	168.09	168.09
Particle images identified as 15R symmetry (no.)	24372	52581	125182
Particle images in helical reconstruction (no.)	24372	52581	125182
Single particles (no.) [c]	365580	788715	1877730
Single particles used (no.) [d]	118273	685161	110600
Overall resolution (Å)	3.3	2.7	3.1
FSC threshold	0.143	0.143	0.143
Kinesin resolution (Å)	3.5	2.9	3.7
Tubulin resolution (Å)	3.3	2.7	3.1
Refinement			
Model composition			
Non-hydrogen atoms	9751	9741	20081
Protein residues	1224	1227	2520
Ligands	5	4	11
R.m.s. deviations			
Bond lengths (Å)	0.0054	0.0068	0.0055
Bond angles (°)	1.16	1.17	1.12
Validation			
MolProbity score	1.32	1.47	1.32
Clashscore	3.54	2.55	2.78
Poor rotamers (%)	0.48	1.61	0.37
Ramachandran plot			
Favored (%)	96.95	95.98	96.28
Allowed (%)	2.97	4.02	3.52
Disallowed (%)	0.08	0.00	0.20

[a] Range of the per-particle defocus estimates. The range corresponds to 90% of the particles used, 5% of the particle defocuses are below and 5% are above this range.
[b] Symmetry imposed during the symmetrical refinement done before the local refinements (rise and twists provided for helical symmetry only).
[c] Total number of particles after symmetry expansion.
[d] Number of asymmetric units, corresponding to a kinesin motor bound to a tubulin dimer, used after 3D classification.

Table 1. Cryo-EM data collection, refinement and validation statistics (3/3)

	MT-KIF1A^{P305L} -ANP-TL$_{012*}$ (EMDB-xxxxx) (PDB xxxx)	**MT-KIF1A^{P305L} -ADP** (EMDB-xxxxx) (PDB xxxx)	**MT-KIF1A^{P305L} -APO** (EMDB-xxxxx) (PDB xxxx)
Data collection and processing			
Magnification (actual)	59242	57078	59242
Voltage (kV)	300	300	300
Electron exposure (e^{-}/Å^2)	49.4	62.9	50.4
Defocus range (μm) [a]	1.0 ; 2.4	0.8 ; 2.0	1.2. ; 2.2
Pixel size (Å)	0.844	0.876	0.844
Symmetry imposed [b]	Helical	Helical	Helical
Rise (Å)	5.64	5.60	5.62
Twist (deg)	168.09	168.09	168.09
Particle images identified as 15R symmetry (no.)	125182	83861	79145
Particle images in helical reconstruction (no.)	125182	83861	79145
Single particles (no.) [c]	1877730	1257915	1187175
Single particles used (no.) [d]	254197	119590	620149
Overall resolution (Å)	3.0	3.0	3.4
FSC threshold	0.143	0.143	0.143
Kinesin resolution (Å)	3.4	3.8[e]	4.1
Tubulin resolution (Å)	3.0	2.9	3.4
Refinement			
Model composition			
Non-hydrogen atoms	20098	9838	9649
Protein residues	2523	1234	1222
Ligands	11	5	3
R.m.s. deviations			
Bond lengths (Å)	0.0053	0.0056	0.0052
Bond angles (°)	1.11	1.17	1.10
Validation			
MolProbity score	1.30	1.31	1.48
Clashscore	2.80	3.31	3.21
Poor rotamers (%)	1.02	0.28	0.29
Ramachandran plot			
Favored (%)	96.56	96.90	94.65
Allowed (%)	3.16	3.02	5.35
Disallowed (%)	0.28	0.08	0.00

[a] Range of the per-particle defocus estimates. The range corresponds to 90% of the particles used, 5% of the particle defocuses are below and 5% are above this range.
[b] Symmetry imposed during the symmetrical refinement done before the local refinements (rise and twists provided for helical symmetry only).
[c] Total number of particles after symmetry expansion.
[d] Number of asymmetric units, corresponding to a kinesin motor bound to a tubulin dimer, used after 3D classification.
[e] Note that the resolution of that kinesin in this class is very heterogeneous and weak and this resolution estimate is dominated by the signal near the microtubule interface.

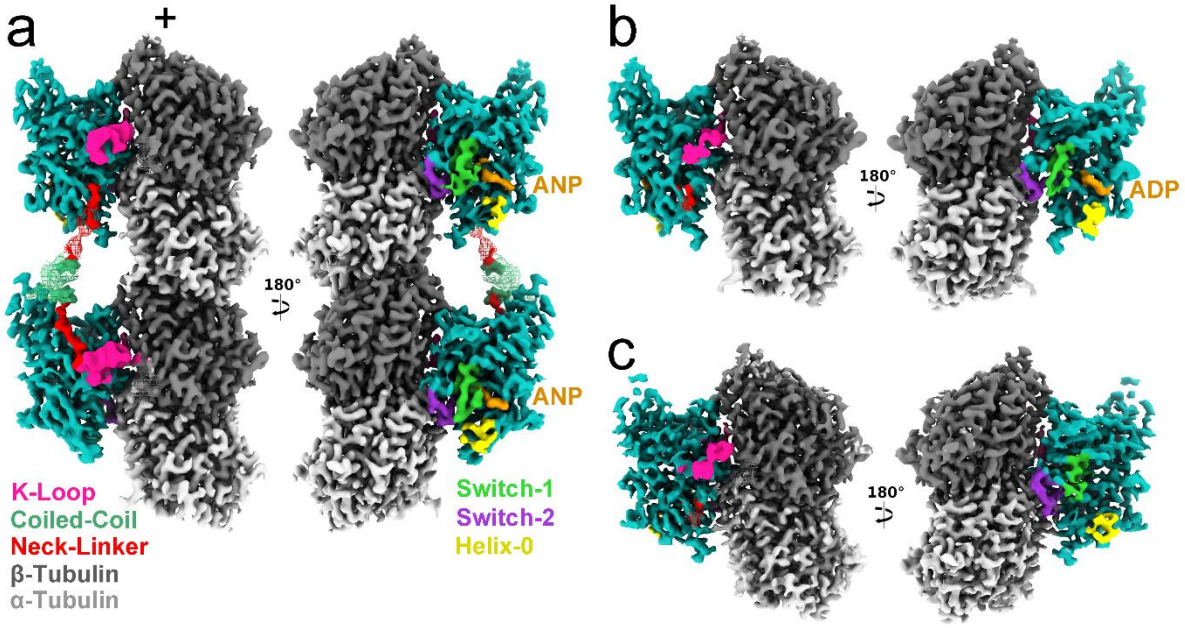

Fig 1. Cryo-EM maps of microtubule bound KIF1A in different nucleotide states. Each panel shows two views of the iso-density surfaces of microtubule-bound KIF1A 3D maps rotated 180° from each other. Surfaces are colored as labeled on the figure, according to the fitted atomic structure they enclose. The signal around the K-loop was low-passed filtered and displayed at a lower contour level than the rest of the map to visualize this mobile part better. The signal near the C-terminal tail of β-tubulin was also low-passed filtered and displayed as a gray mesh at the same contour level as the nearby K-loop area. **a:** Microtubule bound KIF1A with the ATP analogue AMP-PNP (abbreviated as ANP). The map illustrated corresponds to the average two-heads-bound state (MT-KIF1A-ANP-T23L1). The coiled-coil density as well as part of the neck-linker from the leading head were low-pass filtered and displayed as a mesh at a lower contour level than the one of the main map. Densities from the neck-linkers and coiled-coils connecting the two heads are visible. ANP densities are present in both the leading and trailing heads. Note that one-head-bound states were also found in the ANP datasets (Supplementary Fig. 2 & 3). **b-c:** Iso-density surface representations of KIF1A in the ADP and APO states respectively (datasets MT-KIF1A-ADP and MT-KIF1A-APO).

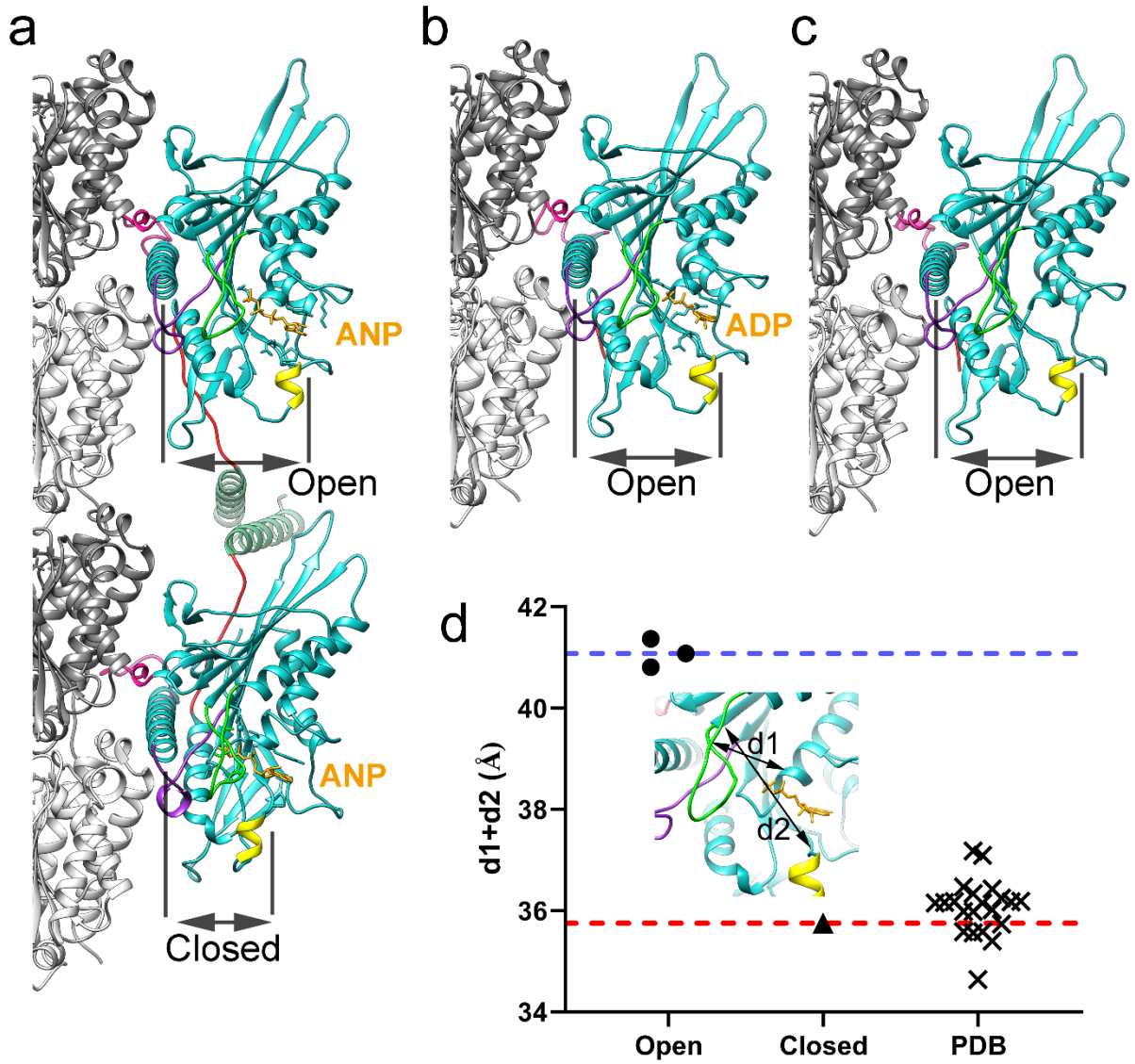

Fig. 2. KIF1A atomic models. **a:** AMP-PNP two-heads-bound state. **b,** ADP one-head-bound state. **c,** Apo one-head-bound state. **d:** Scatter plot of nucleotide binding pocket distances between selected atoms across the KIF1A nucleotide binding pocket (inset). d1 and d2 are the distances between the atomic model coordinates of the CA atoms of KIF1A residues 104-216 and 14-218 respectively. Both distances move in the same direction between motor domain conformations (open, closed or semi-closed) and each data point in the scatter plot corresponds to the added values, d1+d2. Circle symbols in the Open column correspond to the motor domain of the leading head in the open conformation in the AMP-PNP two-heads-bound state model (a), in the ADP model (b) and in the in the Apo model (c). The triangle symbols in the Closed column correspond to the trailing head in the closed conformation in the AMP-PNP two-heads-bound state model (a). The X symbols in the PDB column correspond to KIF1A or KIF1A-MT models deposited in the PDB database with accession codes: 1I5S, 1I6I, 1VFV, 1VFW, 1VFX, 1VFZ, 2HXF, 2HXH, 2ZFI, 2ZFJ, 2ZFK, 2ZFL, 2ZFM, 4EJQ, 4EGX, 7EO9, 7EOB, 1IA0, 2HXF, 2HXH, 4UXO, 4UXP, 4UXR and 4UXS. Dashed horizontal lines mark the average of the data points in the Open

(blue) and Closed (red) columns. All models are oriented with the MT plus-end at the top. Model parts are colored as in Fig. 1.

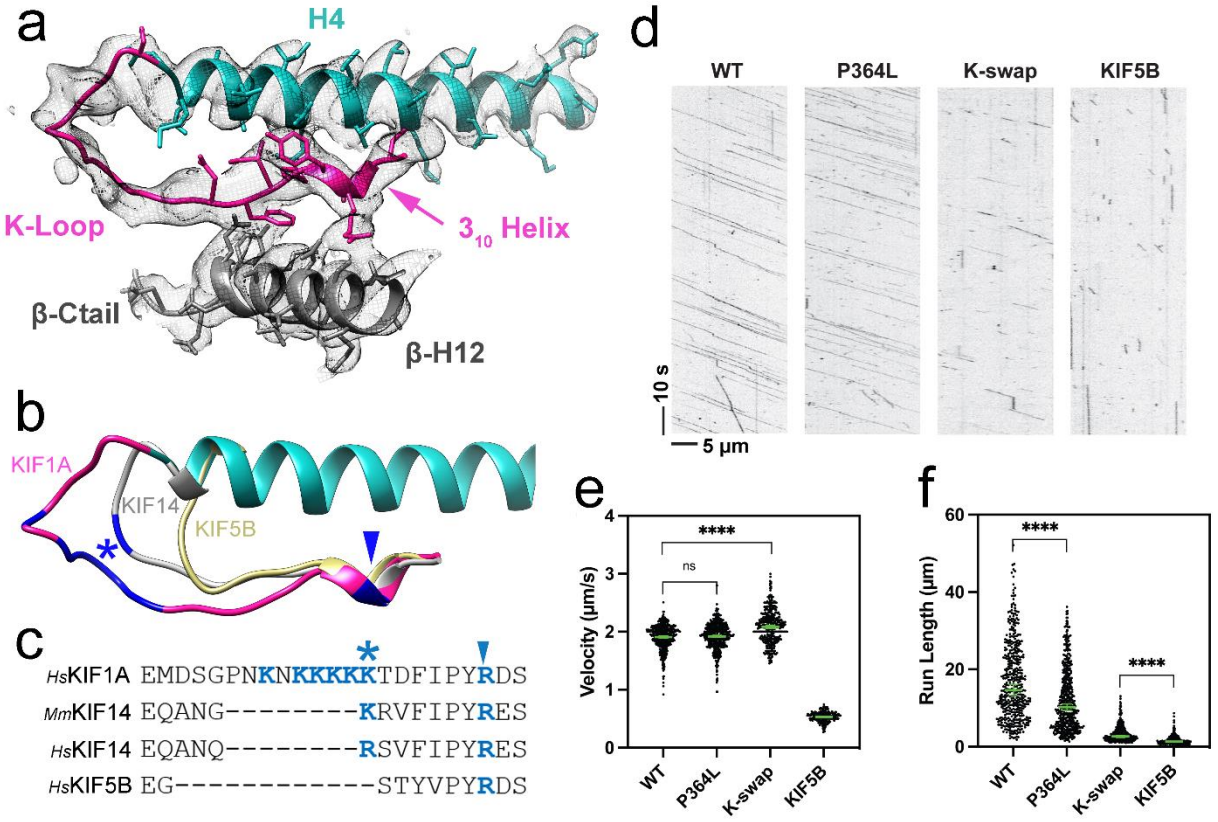

Fig. 3. K-loop structure. a: Area of the K-loop of the KIF1A-ADP model. The model is shown as a ribbon representation with side chain atoms as stick. Parts colored as in Fig. 1. Cryo-EM density map shown as an iso-contour semitransparent mesh. A low pass-filtered version of the map is shown in the K-loop tip area (left-most). Model side chains are not shown in this area. **b:** Comparison of the K-loop structures of *Hs*KIF1A, *Mm*KIF14 (PDB accession code: 6WWM) and *Hs*KIF5B (PDB accession code: 1MKJ). Positive charged residues (K or R) in the K-loop are colored dark blue. The position of a conserved positively charged residue in the Kinesin-3 loop12 is indicated with the * symbol and that of a highly conserved R residue in the kinesin superfamily with the arrowhead symbol. **c:** Loop-12 sequences. Positively charged residue one code letter are colored dark blue. * and arrowhead symbols point to the same residues indicated in the structures shown in (b). **d:** Kymograph examples of WT, P364L, K-swap, and KIF5B. **e:** The velocities of WT, P364L, K-swap, and KIF5B. The green bars represent the mean with 95% confidence interval (CI). WT: 1.91 [1.89, 1.93] µm/s, n=459; P364L: 1.92 [1.90, 1.94] µm/s n=514; K-swap: 2.09 [2.06, 2.11] µm/s n=398; KIF5B: 0.53 [0.52, 0.54] µm/s n=232. The statistics were performed using unpaired t-test with Welch's correction. ****: P<0.0001; ns: P=0.47. At least 3 experiments were performed for each construct. **f:** Run-lengths of WT, P364L, K-swap, and KIF5B. The green bars represent the median with 95% CI. WT: 14.6 [13.3, 16.1] µm; P364L: 10.2 [9.4, 11.0] µm; K-swap: 2.7 [2.4, 2.9] µm; KIF5B: 1.3 [1.2, 1.5] µm. The statistics were performed using Kolmogorov-Smirnov test. ****: P<0.0001. The number of data points are the same as in the velocity graph.

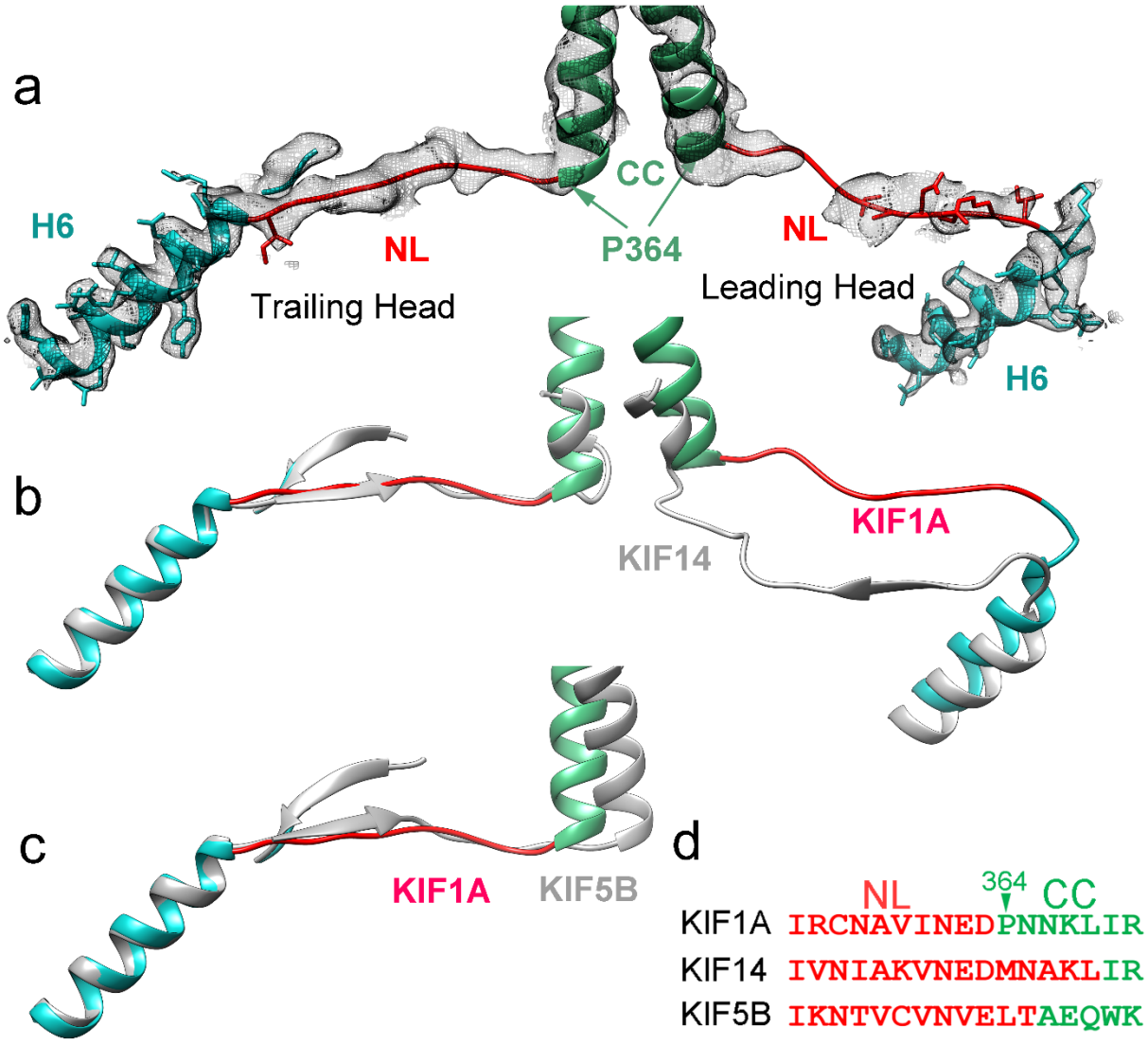

Fig. 4. Neck-Linker structure. a: H6-Neck-Linker (NL) and Coiled coil (CC) area of the KIF1A AMP-PNP two-heads-bound structure. The two-heads-bound structure is shown in ribbon representation with side chain atoms as sticks. Parts colored as in Fig. 1. Cryo-EM density map shown as an iso-contour semitransparent mesh. A low pass-filtered version of the map is shown in the NL and CC area. The model side chains are not shown in this area. **b:** Comparison of the two-heads-bound state structures of KIF1A and KIF14 (grey color, PDB accession code: 6WWL). **c:** Comparison of the KIF1A (trailing head in the two-heads-bound state) and KIF5B with docked NL and CC helix crystal structure (grey color, PDB accession code: 1MKJ). **d:** NL and CC sequences alignment of KIF1A, KIF14 and KIF5B. Residues located in the NL or the CC helix, according to the structures shown in (a) to (c), are colored red and green respectively.

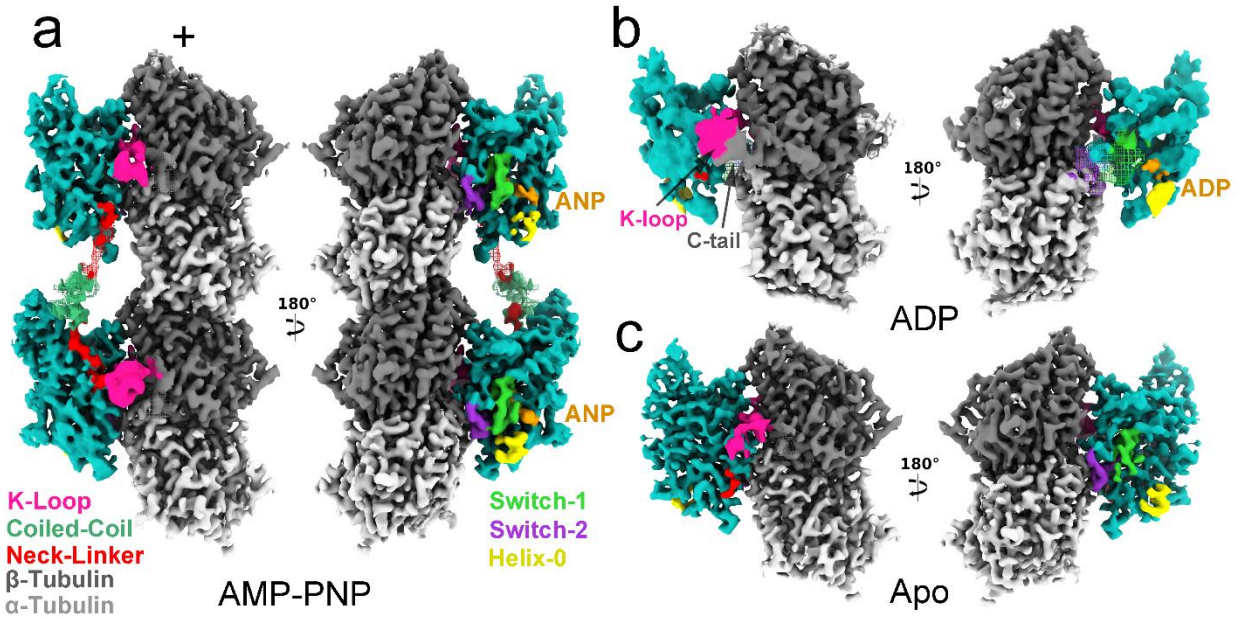

Fig 5. Cryo-EM maps of microtubule bound KIF1A^{P305L} in different nucleotide states. Each panel shows two views of the iso-density surfaces of microtubule-bound KIF1A^{P305L} 3D maps rotated 180° from each other. Surfaces are colored as labeled on the figure, according to the fitted atomic structure they enclose. The signal around the K-loop was low-passed filtered and displayed at a lower contour level than the rest of the map to visualize this mobile part better. **a:** MT-bound KIF1A^{P305L} with ANP. The signal near the C-terminal tail of β-tubulin was also low-passed filtered and displayed as a gray mesh at the same contour level as the nearby K-loop area. The map illustrated corresponds to the two-heads-bound state MT-KIF1A^{P305L}-ANP-TL$_1$. The coiled-coil density as well as part of the neck-linker from the leading head were low-pass filtered and displayed as a mesh at a lower contour level than the one of the main map. Densities from the neck-linkers and coiled-coils connecting the two heads are visible. Like in the KIF1A dataset, in ANP the motor has a major two-heads-bound state as illustrated here, with the trailing head in a closed state and the leading head in an open state with the neck-linker oriented backwards. ANP densities are present in both the leading and trailing heads. Note that one-head-bound states were also found in the ANP datasets (Supplementary Fig. 5). **b:** Iso-density surface representation of KIF1A^{P305L} in the ADP state (dataset MT-KIF1A^{P305L}-ADP). In this map that has lower resolution than the others, the switches area was low pass filtered and displayed as a mesh. The K-loop area and C-terminal tail of β-tubulin have connected densities and were low-passed filtered and displayed as a solid surface. **c:** Iso-density surface representations of KIF1A^{P305L} in the APO state (dataset MT-KIF1A^{P305L}-APO respectively), illustrated as in panel (**a**). Both motors KIF1A^{P305L} in the ADP and APO datasets are in the open conformation like KIF1A (**Fig. 1-2**).

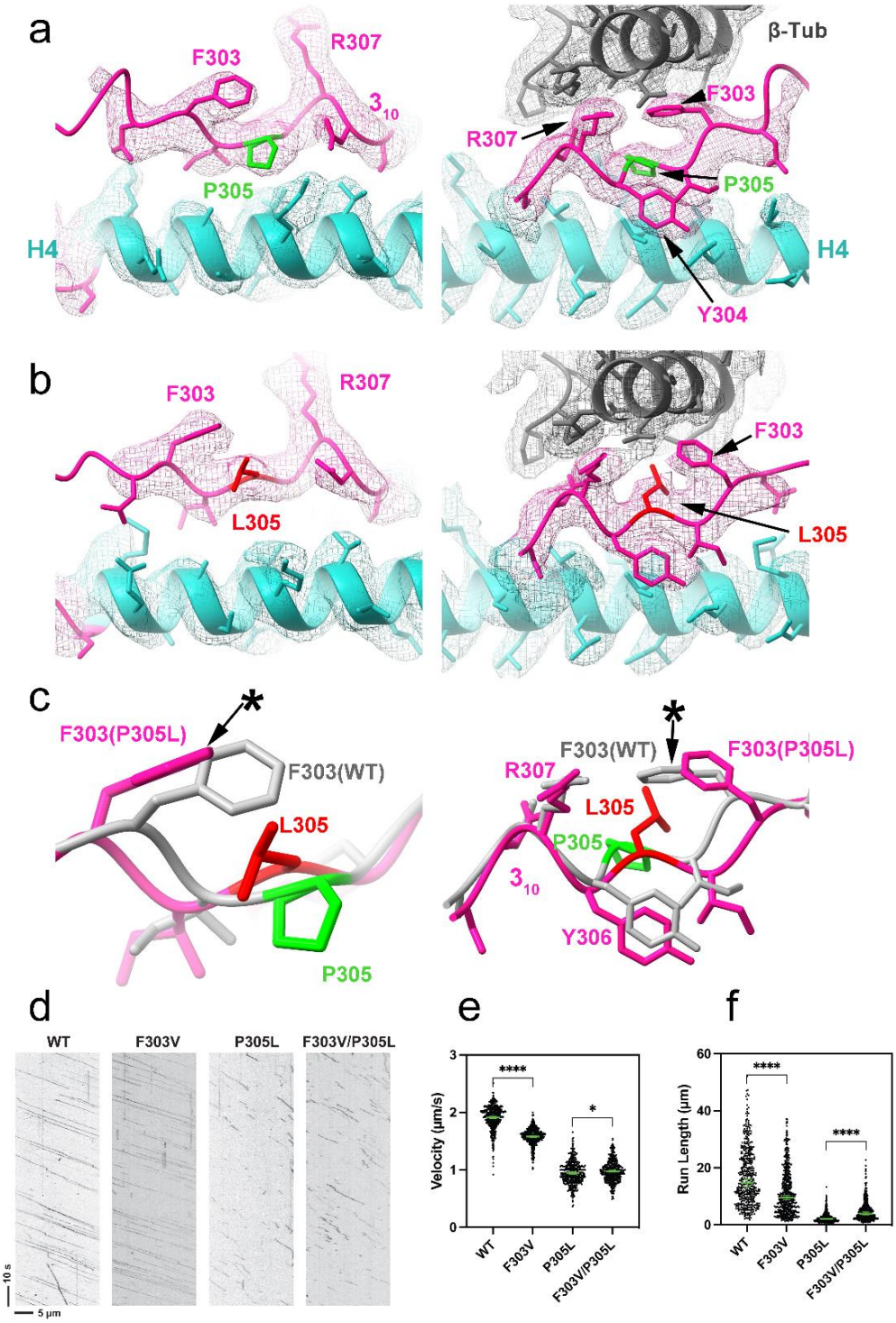

Fig 6. Effect of the P305L mutation on KIF1A structure and activity. a: Iso-density surface representations of the cryo-EM map of WT KIF1A in the ANP state (MT-KIF1A-ANP-$T_{23}L_1$) in the neighborhood of residue P305. The surface is represented as a mesh and colored based on the underlying fitted molecular model (same color convention as in **Fig.1**). The model is shown with

a cartoon representation with displayed side chains. The left and right panels represent two different views of the same area, the left one looking from β-tubulin, on an axis orthogonal to the microtubule axis, and the right one along the microtubule axis, from the (+) end towards the (-) end. All the side chains are resolved in this area, including P305, colored in green. **b:** Iso-density surface representations of the cryo-EM map of KIF1A^{P305L} mutant in the ANP state (MT-KIF1A^{P305L}-ANP-TL$_{012*}$), same view as in (**a**). The side chains are also well resolved in the KIF1A^{P305L}, including L305, colored in red. L305 is positioned differently from P305, with L305 pointing more towards the microtubule interface. **c:** Overlay of the models displayed in (**a**) and (**b**) with the KIF1A WT model displayed in gray, the KIF1A^{P305L} mutant model in pink and the residues 305 colored as in panels (**a-b**). This overlay emphasizes the differences between KIF1A and KIF1A^{P305L} in the neighborhood of residue 305. In addition to a local backbone change at position 305 due to the absence of the proline in L305, the side chain of L305 points towards the F303 of the WT and would clash with this residue if the backbone and side chain of P303 would not change position as observed. The changes up the polypeptide chain after 305 are more modest with the path of the 3-10 helix being very similar, including the position of the highly conserved R307. **d:** Kymograph examples of KIF1A (WT), F303V, P305L, and F303V/P305L. **e:** Distribution of velocities of WT, F303V, P305L, and F303V/P305L. The green bars represent the mean with 95% confidence interval. WT: 1.91 [1.89, 1.93] µm/s, n=459; F303V: 1.58 [1.57, 1.59] µm/s n=557; P305L: 0.95 [0.93, 0.96] µm/s, n=438; F303V/P305L: 0.98 [0.96, 0.99] µm/s n=441. The statistics were performed using unpaired t-test with Welch's correction. ****: P<0.0001; *: P=0.016. At least 3 experiments were performed for each construct. **f:** Run lengths of WT, F303V, P305L, and F303V/P305L. The green bars represent the median with 95% CI. WT: 14.6 [13.3, 16.1] µm; F303V: 9.5 [8.8, 10.3] µm; P305L: 2.0 [1.9, 2.2] µm; F303V/P305L: 3.9 [3.5, 4.4] µm. The statistics were performed using Kolmogorov-Smirnov test. ****: P<0.0001. The number of data points are the same as in the velocity graph (**e**).

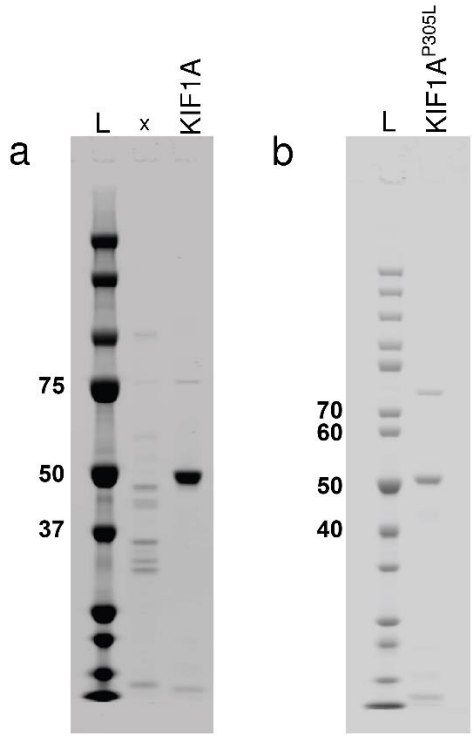

Supplementary Fig 1. Polyacrylamide gel of KIF1A constructs for the cryo-EM assays. a: Gel of KIF1A (KIF1A(aa1-393)-LZ-strepII) ; L: molecular weight standards ; x unrelated sample. **b:** Gel of KIF1A^{P305L}(KIF1A(aa1-393, P305L)-LZ-strepII); L: molecular weight standards.

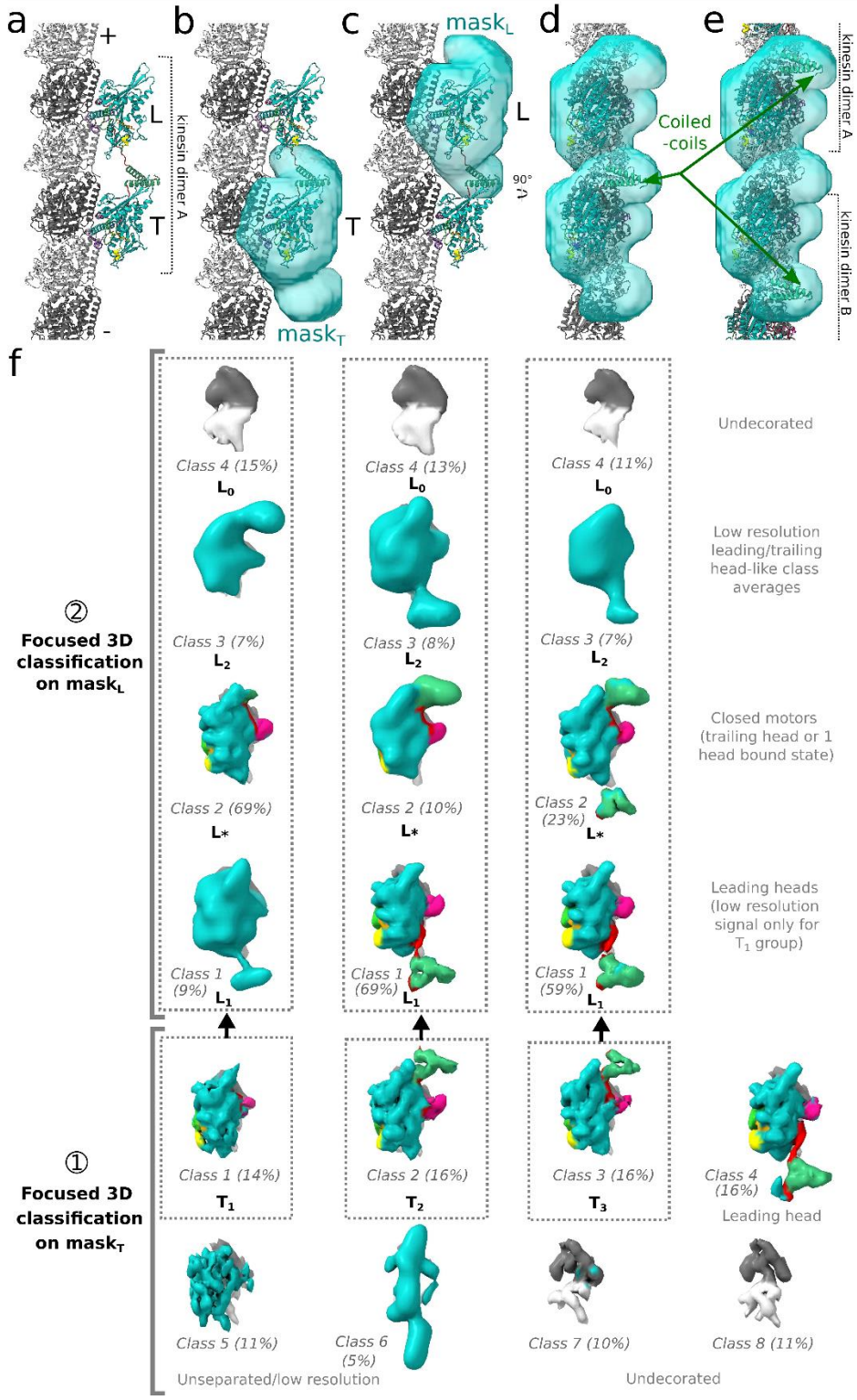

Supplementary Fig 2. 3D classification strategy used for the MT-KIF1A-ANP dataset. a: Model of a KIF1A kinesin dimer ("kinesin dimer A") on a microtubule protofilament. The polarity of the microtubule is indicated. The leading head of the kinesin dimer is indicated by the letter L while the trailing head is indicated by the letter T. Coiled coil is colored green and other colors are

as in **Fig.1**. **b-c:** Semi-transparent surface view of the two masks $mask_T$ (**b**) and $mask_L$ (**c**) used successively during the 3D classification. These two 30 Å resolution masks differ only by their position: $mask_T$ covers the trailing position of the kinesin dimer A (site T, **b**) while $mask_L$ covers it's leading head (site L, **c**), i.e. the next kinesin site on the (+) end on the microtubule protofilament. **d:** 90 degree rotated view of the kinesin dimer model of panel (**a**) with both $mask_T$ and $mask_L$ displayed. **e:** Same view as (**d**) with 2 consecutive two-heads-bound kinesin dimers A and B attached to the microtubule protofilament but with a registration off by 82 Å (length of tubulin dimer) compared to the kinesin dimer A shown in (**a-e**). Note that both masks cover the area occupied by the coiled-coil densities for the two types of registrations displayed in (**e**) and (**d**). **f:** Scheme representing the classification strategy used for the MT-KIF1A-ANP dataset using the $mask_T$ and $mask_L$ illustrated in (**a-e**). All the class averages displayed in the panel correspond to the 3.5Å/pixel ones produced by the 3D classifications, with the same viewing orientation as in panels (**d-e**). First, a 3D classification in 8 classes and focusing on $mask_T$ was performed (step ①). This led to the 8 class averages displayed on the lower part of the figure. The classes 1-3 correspond to kinesin motors in closed states with the neck-linker docked and obtained in similar propensities (see Supplementary Fig. 3 for a side view of these three classes at full resolution) and were named T_1, T_2 and T_3. Class 4 corresponds to a leading head with an undocked neck-linker pointing backwards and connected to a coiled-coil. Class 5 is decorated by a kinesin but it's state couldn't be assigned, and it likely represents particle for which the state has not been separated, unlike particles from the classes 1 to 4. Classes 6 is a low-resolution class which state couldn't be assigned, while classes 7 and 8 are undecorated. By virtue of the symmetry expansion used, the leading heads of the 2-heads-bound state as seen in class 4 will be also present on site L and since only the classes T_1, T_2 and T_3 could correspond to two-heads-bound state kinesin dimers with their leading head on the site L, these three classes were further classified on site L. In the second classification step (step ②) focusing on $mask_L$, the particles from each of the classes T_1, T_2 and T_3 were classified in 4 classes. The related class averages are displayed. The class averages fell into 4 groups as annotated on the figure, with some differences in relative frequencies. Each of T_1, T_2 and T_3 have a major class at position L (containing respectively 69%, 69% and 59% of their particles). That major class is a motor in a closed state (i.e. belonging to another kinesin dimer) for T_1 (class-2 in T_1 classification at site L with $mask_L$) named L_*. Note that unless the kinesin coiled-coil would unfold the motor seen on the site L must correspond to another kinesin molecule, meaning that the kinesin motor on site T from class T_1 and class L_* (abbreviated T_1L_*) are in a single-head-bound state. Unlike T_1, for T_2 and T_3 the major class on site L is a connected leading head i.e., belonging to a two-heads-bound kinesin state. These classes with connected leading heads were named L_1. In the T_1 classification on site L only a weak and low resolution class bears similarity with a leading head (Class 1, named L_1 ; see also Supplementary Fig. 3 for a full size reconstruction of this class) so T_1L_1 does not appear as a pure two-heads-bound state class as T_2L_1 and T_3L_1. Each of the classifications of the site L from T_2 and T_3 also show a class (class 2) corresponding to motors in a closed state with a coiled-coil density towards the (+) end of the motor (see also Supplementary Fig. 3). Like in the T_1 classification these classes were named L_* and they indicate the presence of one-head-bound-states on the T site. For each of the classifications on site L from T_1, T_2 and T_3, other lower resolution classes leading- or trailing-head-like were obtained (classes 3, named L_2) as well as empty sites (classes 4, named L_0) without kinesin densities. These empty sites on site L also indicate that the corresponding motors on site T (classes T_1L_0, T_2L_0 and T_3L_0) are in a single head bound state.

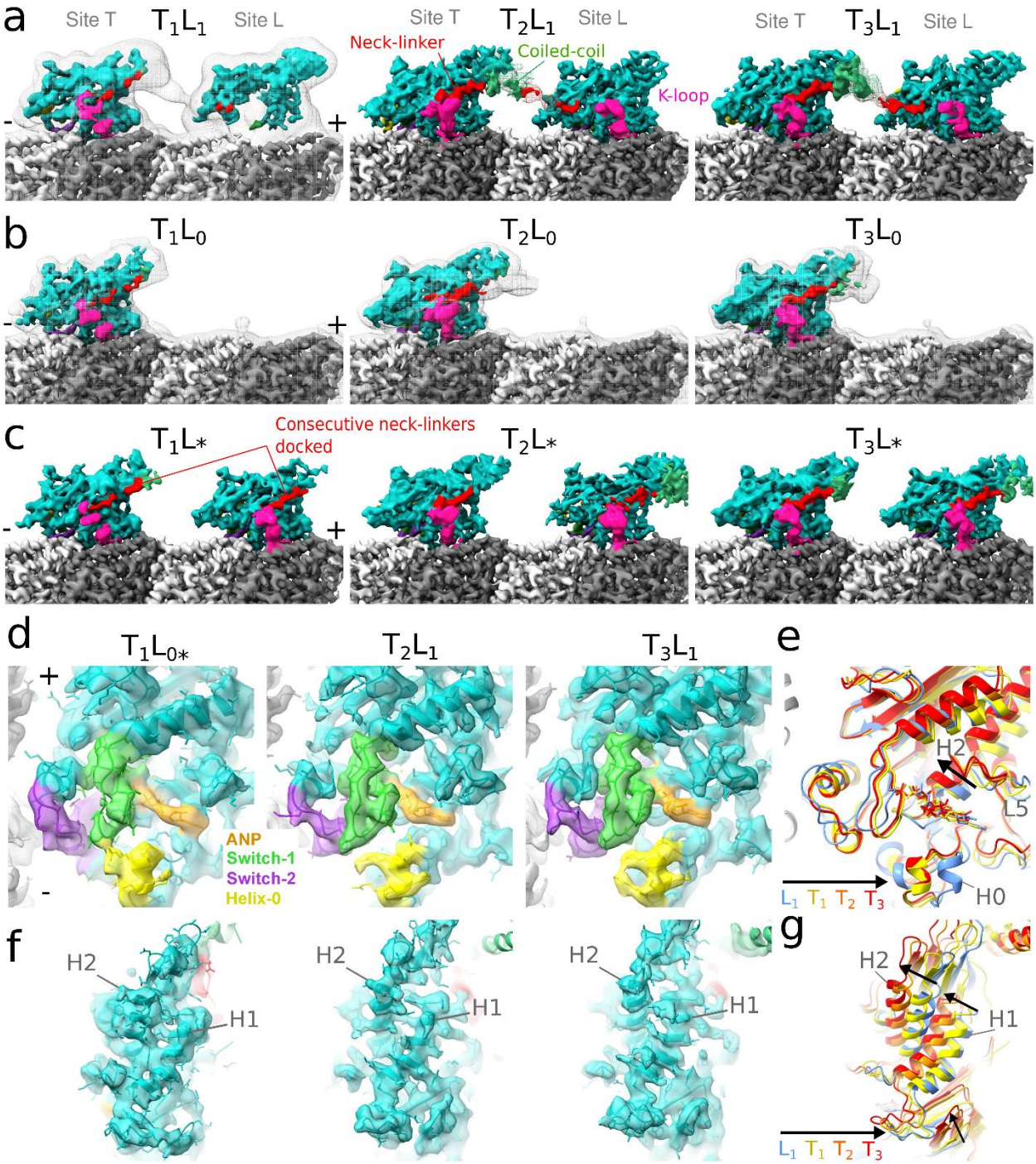

Supplementary Fig 3. Multiple binding modes and conformational states of KIF1A-ANP. a-c: Iso-density surface representations of the cryo-EM maps from the KIF1A-ANP dataset for the classes T_1L_1, T_2L_2 and T_3L_3 (**a**), T_1L_0, T_2L_0 and T_3L_0 (**b**), T_1L_*, T_2L_* and T_3L_*. **c**: The color scheme is the same as the one used in **Fig.1**. The microtubule protofilament polarity are indicated. The signal around the K-loop was low-passed filtered and displayed at a lower contour level than the rest of the map to visualize this mobile part better. In (**a**) note that the motor domain at site T has a weaker signal than the one at site L. Only by low-pass filtering this class average, as shown with a gray mesh, a signal of connectivity between the two heads is seen. The small T_1L_1 class (accounting for 9% of the site L classification of the T_1 class) appears therefore to be a

heterogeneous class which cannot be assigned as being only a two-heads-bound state. Since the other T_1 classes are in a one-head-bound state, the large majority of the T1 motors are therefore in a one-head-bound state (unlike T_2 and T_3). In T_2L_1 and T_3L_1, the coiled-coil density as well as part of the neck-linker from the leading head were low-pass filtered and displayed as a mesh at a lower contour level than the one of the main map. T_2L_1 and T_3L_1 are both two-heads-bound state, as indicated by the densities of the coiled-coil as well of both neck-linkers positioned in opposite orientations. Note the increasing density of the inter-head connection (neck-linker and coiled-coil) from T_1L_1 to T_2L_1 to T_3L_1, in these classes that account for 1.3 %, 10.9 % and 9.8 % of the particles of the MT-KIF1A-ANP dataset respectively. The class average of T_3L_1 has the strongest inter-head connection density (neck-linker and coiled-coil) in the MT-KIF1A-ANP dataset despite having less particles than T_2L_1, suggesting a more rigid conformation than T_2L_1. In (**b**) the densities of T_1L_0, T_2L_0 and T_3L_0 are displayed overlayed with a low-pass filtered versions of these maps. These maps show a lack of kinesin density at site L, indicating that the motors detected on the site T are one-head-bound states. In (**c**), each of T_1L_*, T_2L_* and T_3L_* classes show a docked neck-linker in both sites T and L, also indicating that the motors detected on the sites T are one-head-bound states (and that the motor seen on the site L corresponds to another kinesin dimer). **d-g:** Comparison of the conformation of the three detected KIF1A trailing heads conformations T_1, T_2 and T_3. For this comparison the maps of the one-head-bound-states T_1L_{0*}, and of the two-heads-bound states T_2L_1 and T_3L_1 were used. In (**d**), semi-transparent iso-density surfaces of the nucleotide binding area of the kinesin are shown with the underlying models displayed with a cartoon representation. These T_1, T_2 and T_3 models are overlayed with the same viewing angle in (**e**) and colored yellow, orange and red respectively as indicated. Additionally, the model of the leading head L_1 (from $T_{23}L_1$) is displayed in blue for comparison. T_1, T_2 and T_3 share the same H0 position typical of a closed state, and distinct from the one of the open states found in L_1. Note that the position of H2 close to the nucleotide and of loop-5 (L5) follow the order L_1, T_1, T_2, T_3 which is indicated with a black arrow. This trend corresponds to a progressive closing of the nucleotide binding pocket with the nucleotide inserted further in the pocket. This gradient of conformation is more dramatically visible on the full helices H1 and H2. Panels (**f-g**) show a similar comparison as in (**d-e**) but focusing on these two helices. Arrows on the model overlay in (**g**) emphasize the gradation of motor closing from L_1 to T_3. Note that T_2 and T_3 are the most similar among these 4 states, while T_1 despite being a closed state with a docked neck-linker (**b-c**) appears as the closest to an open state (L_1) in several areas like near helices H1 and H2. Importantly, T_1 being a major conformation of the MT bound head of KIF1A in the one-head-bound state (12% of the dataset in T_1 (T_1L_{0*}) vs 4% for T_2 (T_2L_{0*}) and 6% for T_3 (T_2L_{0*}) are in one-head-bound states, Supplementary Fig. 2) but at best the least populated conformation in the two-heads-bound state (< 1.3% (T_1L_1) vs 11% for T_2 (T_2L_1) and 10% for T_3 (T_3L_1)), these structural observations indicate that binding of the leading head restricts the conformation of the trailing head to more close ones (T_2 and T_3) which are presumably more favorable for ATP hydrolysis. This property of KIF1A to have the dynamic nucleotide binding pocket of the MT bound head partially closed in the one-head-bound-state and further closed once the leading head binds is possibly related to its high processivity.

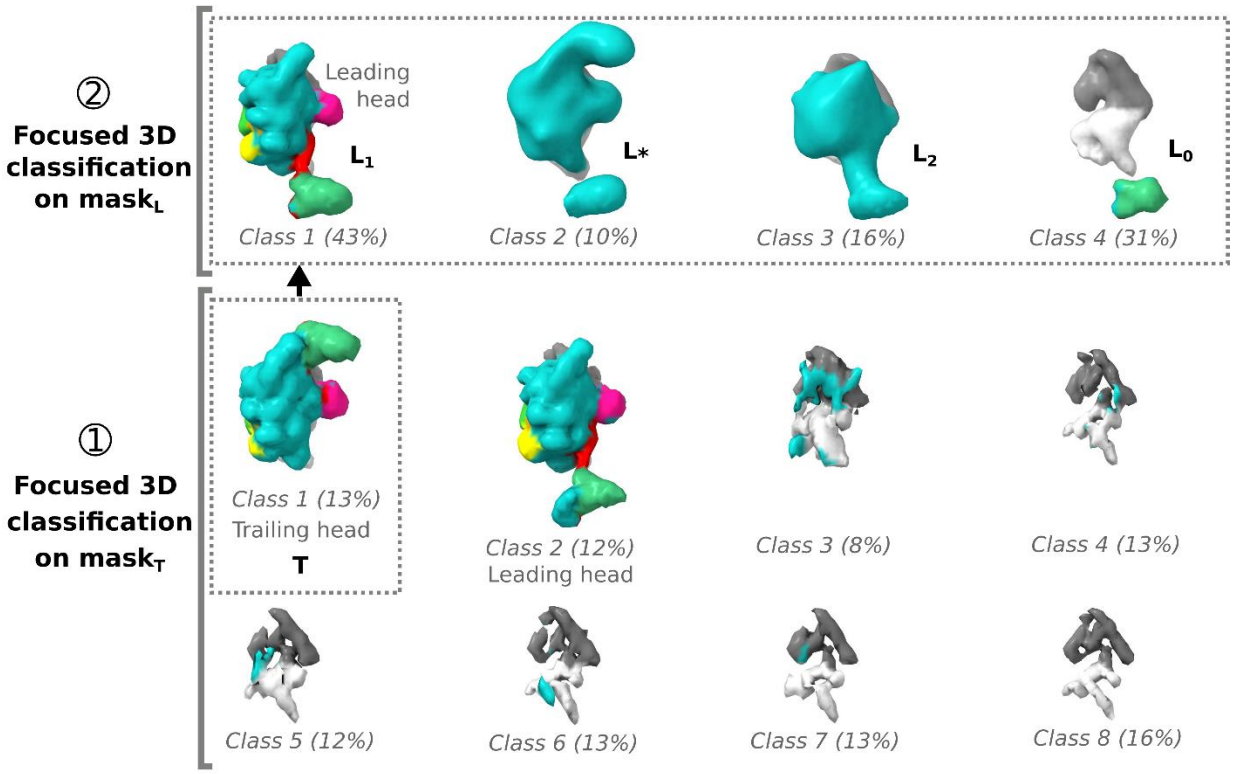

Supplementary Fig 4. 3D classification strategy used for the MT-KIF1A^{P305L}-ANP dataset. The same 3D classification strategy used for the MT-KIF1A-ANP was used for the MT-KIF1A^{P305L}-ANP dataset. The first 3D classification in 8 classes focusing on mask$_T$ (step ①) led to the 8 class averages displayed on the lower part of the figure. Class 1 corresponds to kinesin motors with the coiled-coil density detected towards the (+) end of the motor (forward) while class 2 corresponds to a leading head with the undocked neck-linker connected to a coiled-coil present towards the (-) end of the motor domain (backwards). All the other 6 classes appear undecorated by a kinesin. The single class with a closed state was named class T, and following the same strategy as in the MT-KIF1A-ANP dataset, it was further classified in step ② in 4 classes on the site L (with mask$_L$). The corresponding 4 class averages are displayed in the upper part of the figure. The major class (class 1) corresponds to a motor in the leading head conformation with an undocked neck-linker pulled backwards and connected to a coiled-coil which density is visible. The class TL_1 therefore corresponds to a two-heads-bound kinesin state. The classes 2 and 3 at low resolution bear similarities with a trailing and leading head respectively and were named L_* and L_2 but could not be assigned to these specific states as reliably as the class 1 L_1. Class 4 is undecorated so the corresponding motors on the site T (class TL_0) are in a single head bound state (no leading head bound forward).

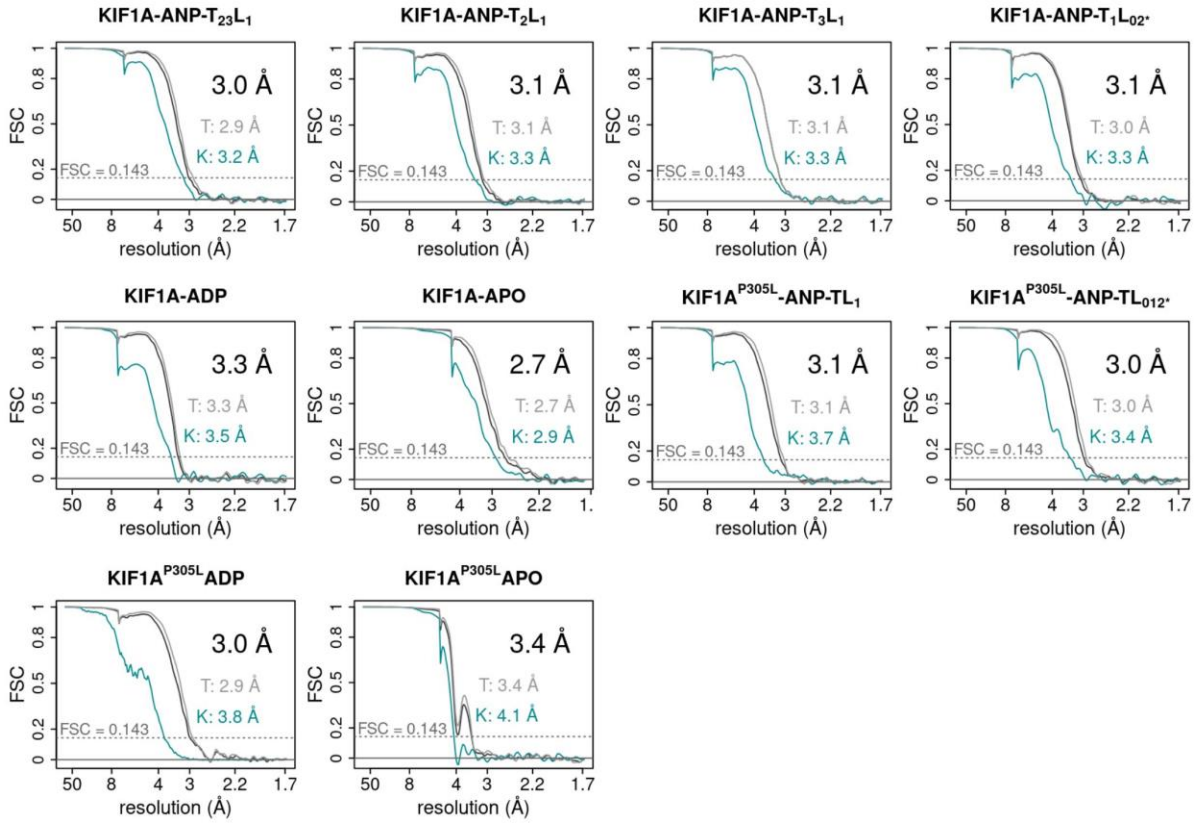

Supplementary Fig 5. Resolution estimation of the cryo-EM maps. FSC curves of KIF1A structures solved by cryo-EM. Overall FSC in black, tubulin part FSC in grey and kinesin part FSC in turquoise. Resolution values ($FSC_{0.143}$) for the overall, tubulin (T) and kinesin (K) parts are indicated. Half maps and masks used to generate the FSC curves are deposited in the EMDB (accession numbers in Table 1).

Dataset	Kinesin concentration (µM)	Buffer	Decorated (%)	Undecorated (%)	Unknown (%)
MT-KIF1A-ANP	20	BRB80	74	21	5
MT-KIF1A-ADP	40	BRB80	32	39	29
MT-KIF1A-APO	40	BRB80	95	0	5
MT-KIF1A^{P305L}-ANP	40	BRB36	25	75	0
MT-KIF1A^{P305L}-ADP	40	BRB36	9	86	5
MT-KIF1A^{P305L}-APO	40	BRB36	91	9	0

Supplementary Table 1. Levels of decoration in each of the cryo-EM dataset. The decorated fraction corresponds to the fraction of the particles-images assigned to classe(s) for which the class average(s) after the focused 3D classification on the single kinesin site (or site T for ANP datasets) shows a density that could be recognized as being a kinesin head bound on the tubulin dimer. The undecorated fraction corresponds to class averages showing a lack of kinesin present on the tubulin dimer. In most datasets there are some low resolution classes (like class 6 in Suplementary Fig 2) for which the class averages show a density that was not reliably assigned as decorated or undecorated and such cases are listed as unknown in the table.

Dataset	$f[\mathrm{2HB}]$ (%)	$f[\mathrm{1HB_{all}}]$ (%)	$f[\mathrm{1HB_{free}}]$ (%)	$\frac{f[\mathrm{2HB}]}{f[\mathrm{1HB_{all}}]+f[\mathrm{2HB}]}$ (%)	$\frac{f[\mathrm{2HB}]}{f[\mathrm{1HB_{free}}]+f[\mathrm{2HB}]}$ (%)
MT-KIF1A-ANP	12	21	6	36	67
MT-KIF1A^{P305L}-ANP	6	4	4	58	58

Supplementary Table 2. Comparison of the frequencies of one-head-bound state and two-heads-bound state in the MT-KIF1A-ANP and MT-KIF1A^{P305L}-ANP datasets. The table reports the observed two-heads-bound (2HB) state frequency f[2HB], the one-head-bound (1HB) state frequency f [$1HB_{all}$] (corresponding to all the one-head-bound states detected) and the one-head-bound state unconstrained frequency f[$1HB_{free}$] (corresponding to particles for which an empty site is present at site L (Supplementary Fig 2 & 3). All frequencies are given as percentages. All the class frequencies for these two datasets are available in Supplementary Fig 2 and 4. Classes with associated class averages at low resolution and/or for which the one-head-bound or two-heads-bound state status is unclear are not included in these estimates. For the MT-KIF1A-ANP dataset, the classes frequencies combined to estimate the frequency of all the one-head-bound states ($1HB_{all}$) are T_1L_*, T_1L_0, T_2L_*, T_2L_0, T_3L_*, T_3L_0 ; for the one-head-bound state unconstrained ($1HB_{free}$) these classes are T_1L_0, T_2L_0 and T_3L_0 and for the two-heads-bound state these classes are T_2L_1 and T_3L_1. For the MT-KIF1A^{P305L}-ANP dataset, the class used to estimate the frequency of all the one-head-bound states is $1HB_{all}$, the one used for the one-head-bound state unconstrained ($1HB_{free}$) is TL_0 ; and for two-heads-bound state the class used is TL_1. Two ratios between these frequencies are given, the right-most one aims to partially account for the large decoration differences between these two datasets (MT-KIF1A-ANP : 74 % ; MT-KIF1A^{P305L}-ANP : 25 %, Supplementary Table 1).